

KRITIKA SUMMER PROJECTS 2024

Constraining Axion Miniclusters and Primordial black holes using gravitational Microlensing

Akshank Tyagi, Chirag Sharma, Suryansh Srijan,
Mehul Goyal, and
Mentor: Manish Tamta

KRITTIKA SUMMER PROJECTS 2024

Constraining Axion Miniclusters and Primordial black holes using gravitational Microlensing

Akshank Tyagi¹, Chirag Sharma², Suryansh Srijan³, Mehul Goyal⁴, and
Mentor: Manish Tamta⁵

¹Indian Institute of Science Bangalore

²Indian Institute of Science Education and Research Bhopal

³Indian Institute of Technology Bombay

⁴Indian Institute of Technology Bombay

⁵Indian Institute of Science Bangalore

Copyright © 2024 Krittika IITB

PUBLISHED BY KRITTIKA: THE ASTRONOMY CLUB OF IIT BOMBAY

KRITTIKA IITB

Project Repository:

Constraining Axion Miniclusters and PBH using Microlensing

First Release, August 2024

Second Release, September 2024

Abstract

Dark matter remains one of the most enigmatic components of the universe, constituting approximately 27% of its total mass-energy content. Despite its significant gravitational influence on cosmic structures, dark matter's elusive nature has prevented its direct detection.

Among the proposed candidates for dark matter, QCD Axions are particularly compelling due to their theoretical origins in the solution to the strong CP problem in quantum chromodynamics. This project explores the potential of detecting QCD axion miniclusters through gravitational microlensing, a phenomenon where a massive object acts as a lens (due to curvature of space-time near it) and magnifies the light from a background source.

Our project makes a brief introductory study of gravitational lensing and microlensing events. Further on we discuss the four most prominent Dark matter Candidates: QCD Axions, Primordial Black Holes, Weakly Interacting Massive Particles and Ultra Light or Fuzzy Dark matter. Then We move to reproducing the result of the paper Fairbairn et. al. (2017)

- Akshank Tyagi

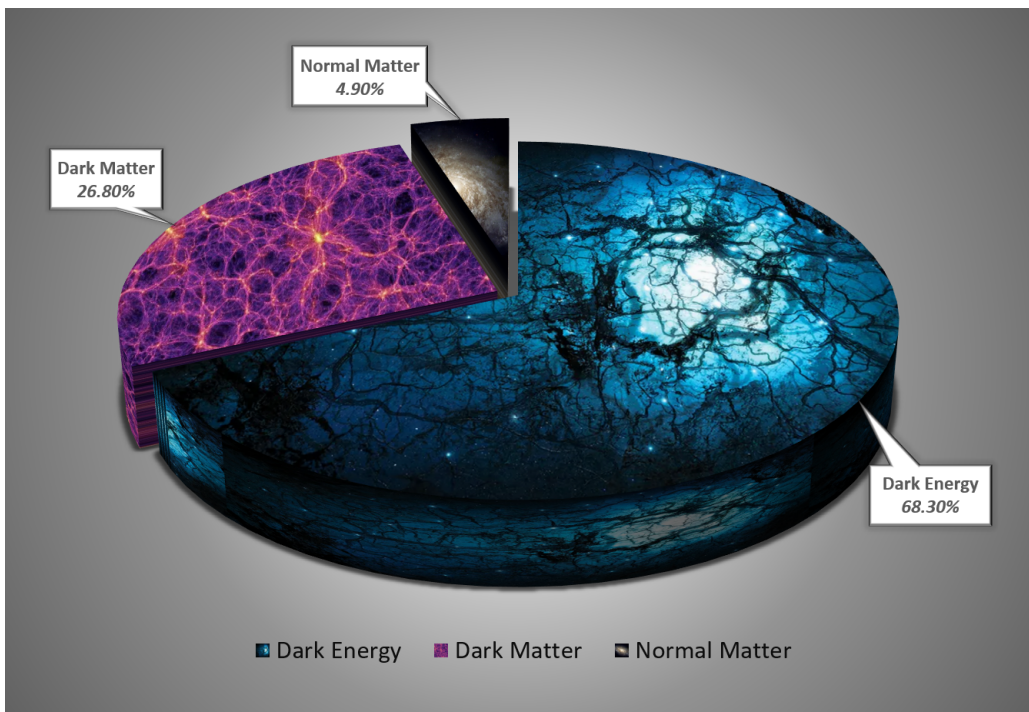


Figure 1: Cosmic Energy Density, Pie Chart from Planck 2013 data, Image credits²

²DE: Tobias Roetsch/All About Space Magazine;
DM: Cosmic Web from the Millennium Simulation/MPA;
NM: NGC 4414 imaged by HST 1995/NASA



Contents

I

Part One

1	Gravitational Lensing	7
1.1	Brief History	7
1.2	Deflection	7
1.3	Lens Equation	9
1.4	Gravitational Microlensing	11
1.4.1	Imaging a Point Source by a Point Mass Lens	11
1.4.2	Magnification	11
1.4.3	Light Curve	12
1.5	Microlensing Simulation 1	13
1.6	Microlensing Simulation 2	14
2	Dark Matter Candidates	17
2.1	Introduction	17
2.1.1	What do we know about dark matter ?	17
2.2	QCD Axion	18
2.2.1	The Standard Model	18
2.2.2	CPT Symmetry	19
2.2.3	Spontaneous Symmetry Breaking and Higgs Mechanism	20
2.2.4	Peccei-Quinn Symmetry	21
2.2.5	Nambu-Goldstone Bosons	21
2.2.6	QCD Cross Over	21
2.2.7	Axion Dark Matter	22

2.3	Primordial Black Holes	24
2.3.1	Formation of PBH	24
2.3.2	Observing Signatures of PBH	26
2.4	Weakly Interacting Massive Particles	28
2.4.1	What exactly are Weakly Interacting Massive particles?	28
2.4.2	Freeze-out Mechanism	28
2.4.3	WIMP Miracle	29
2.4.4	Supersymmetry	29
2.4.5	Lightest Neutralino of SUSY	30
2.4.6	Experimental Situation	30
2.4.7	Direct Detection	30
2.5	Ultra Light Dark Matter	31
2.5.1	Discrepancies at Small Scales in Λ CDM	31
2.5.2	Bose-Einstein condensates and Super-fluids	33
2.5.3	ULDM Model	33

II

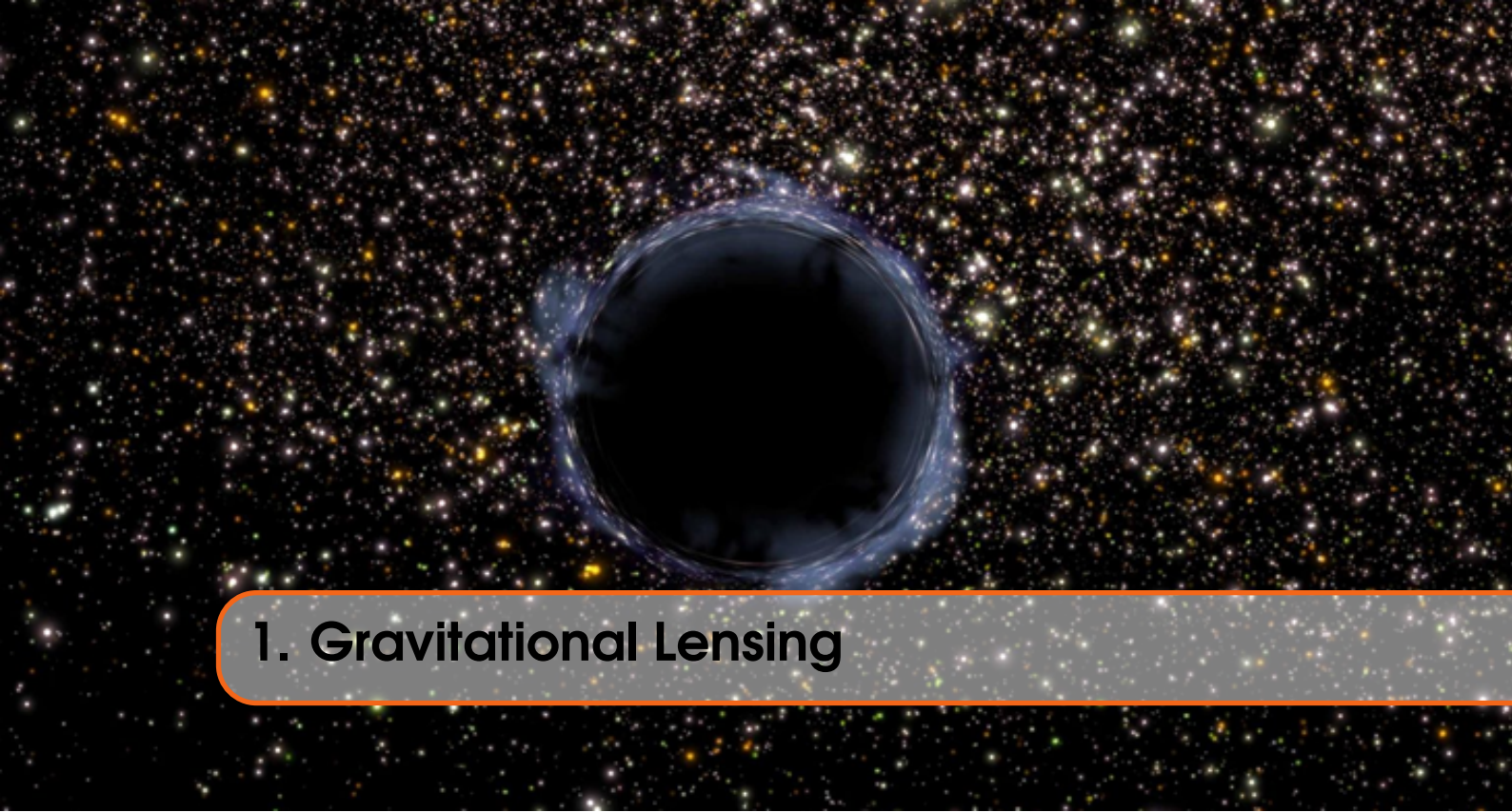
Part Two

3	Axion Miniclusters and their Microlensing signal	39
3.1	Evolution of Axion Field	39
3.2	Axion Miniclusters	40
3.3	Constraining Miniclusuter Mass Function	40
3.3.1	Universal Expansion	41
3.3.2	Calculating T_{osc}	41
3.3.3	Relating F_a and m_a	42
3.3.4	Calculating Miniclusuter Mass	43
3.4	Miniclusuter Density Functions	45
3.4.1	Surface Density Profile $\Sigma(R)$	45
3.4.2	Cumulative Mass Profile $M(< R)$	46
3.5	Theroetical uncertainties in the MCH mass function and analytic results	47
	Bibliography	49
	Articles	49



Part One

1	Gravitational Lensing	7
1.1	Brief History	
1.2	Deflection	
1.3	Lens Equation	
1.4	Gravitational Microlensing	
1.5	Microlensing Simulation 1	
1.6	Microlensing Simulation 2	
2	Dark Matter Candidates	17
2.1	Introduction	
2.2	QCD Axion	
2.3	Primordial Black Holes	
2.4	Weakly Interacting Massive Particles	
2.5	Ultra Light Dark Matter	



1. Gravitational Lensing

1.1 Brief History

The phenomenon of bending of light due to the presence of objects along its path to an observer is termed gravitational lensing. The amount of deflection caused by Sun on starlight was first calculated by Soldner in 1801 using Newtonian gravity and assuming that light is made of corpuscles traveling at the speed of light.

In 1911, Einstein did the calculation again using his Theory of Special Relativity and got the same result. But in 1916 on using the full General Relativity equations, he found the deflection amount to be twice of what he (and Soldner) found earlier. In an expedition led by Sir Arthur Eddington in 1919, the observations were found to agree with Einstein's calculations.

1.2 Deflection

In this section, we will derive Einstein's result for the amount of deflection using Fermat's principle.

Traveling in a medium with refractive index n , the speed of light becomes $v = c/n$. Then, for a fixed distance d we can find the time taken by light to travel through the medium as

$$t_{\text{medium}} = \frac{d}{v} = \frac{n}{c}d \quad (1.1)$$

Then, by Fermat's principle, this time is extremal, which means its variation vanishes

$$\delta \int_A^B n(\vec{x}(l)) dl = 0 \quad (1.2)$$

To proceed, we need to find the form of the refractive index n , and for this, we use a form of the Schwarzschild metric¹

$$ds^2 = \left(1 + \frac{2\Phi}{c^2}\right) c^2 dt^2 - \left(1 - \frac{2\Phi}{c^2}\right) (d\vec{x})^2 \quad (1.3)$$

For light, $ds = 0$,

$$\left(1 + \frac{2\Phi}{c^2}\right) c^2 dt^2 = \left(1 - \frac{2\Phi}{c^2}\right) (d\vec{x})^2 \quad (1.4)$$

Then, the speed of light in gravitational field is

$$v = \frac{|d\vec{x}|}{dt} = c \sqrt{\frac{1 + \frac{2\Phi}{c^2}}{1 - \frac{2\Phi}{c^2}}} \approx c \left(1 + \frac{2\Phi}{c^2}\right) \quad (1.5)$$

where we have used the approximation $\Phi/c^2 \ll 1$. The refractive index is

$$n = \frac{c}{v} = \frac{1}{1 + \frac{2\Phi}{c^2}} \approx 1 - \frac{2\Phi}{c^2} \quad (1.6)$$

To solve the variational problem, we choose an affine parameter λ to parameterize the path of the light such that

$$dl = \left| \frac{d\vec{x}}{d\lambda} \right| d\lambda \quad (1.7)$$

which gives

$$\delta \int_{\lambda_A}^{\lambda_B} d\lambda n[\vec{x}(\lambda)] \left| \frac{d\vec{x}}{d\lambda} \right| = 0 \quad (1.8)$$

Defining the Lagrangian

$$L(\dot{\vec{x}}, \vec{x}, \lambda) = n[\vec{x}(\lambda)] \left| \frac{d\vec{x}}{d\lambda} \right| \quad (1.9)$$

where the dot denotes the derivative with respect to the affine parameter λ , and we have

$$\left| \frac{d\vec{x}}{d\lambda} \right| = |\dot{\vec{x}}| = (\dot{\vec{x}}^2)^{1/2} \quad (1.10)$$

which allows us to use Euler-Lagrange equations

$$\frac{d}{d\lambda} \frac{\partial L}{\partial \dot{\vec{x}}} - \frac{\partial L}{\partial \vec{x}} = 0 \quad (1.11)$$

Now,

$$\frac{\partial L}{\partial \vec{x}} = |\dot{\vec{x}}| \frac{\partial n}{\partial \vec{x}} = (\vec{\nabla} n) |\dot{\vec{x}}| \quad (1.12)$$

$$\frac{\partial L}{\partial \dot{\vec{x}}} = n \frac{\dot{\vec{x}}}{|\dot{\vec{x}}|} \quad (1.13)$$

¹The metric signature is mostly negative and Φ is Newton's gravitational potential.

The vector $\dot{\vec{x}}$ is a tangent vector to the light path and for some suitable choice of the parameter λ , we can assume it to be normalized i.e. $|\dot{\vec{x}}| = 1$. We represent the unit tangent vector to the light path as $\vec{e} = \dot{\vec{x}}$. From this, we get,

$$\frac{d}{d\lambda}(n\vec{e}) - \vec{\nabla}n = 0 \quad (1.14)$$

$$\Rightarrow n\dot{\vec{e}} = \vec{\nabla}n - \vec{e}(\vec{\nabla}n \cdot \vec{e}) \quad (1.15)$$

The second term on the right-hand side of the last equation is the derivative along the light path and thus the whole right-hand side is the gradient of n perpendicular to the light path.

$$\dot{\vec{e}} = \frac{1}{n}\vec{\nabla}_\perp n = \vec{\nabla}_\perp \ln n \quad (1.16)$$

Using the approximation $\Phi/c^2 \ll 1$, we get $\ln n \approx -2\Phi/c^2$, which gives us

$$\dot{\vec{e}} \approx -\frac{2}{c^2}\vec{\nabla}_\perp \Phi \quad (1.17)$$

The total deflection angle of the light path can be written as integral over $-\dot{\vec{e}}$ along the light path

$$\hat{\alpha} = \frac{2}{c^2} \int_{\lambda_A}^{\lambda_B} \vec{\nabla}_\perp \Phi d\lambda \quad (1.18)$$

For a light ray that is going in z -direction and passes a lens at $z = 0$ with impact parameter b , the deflection angle becomes

$$\hat{\alpha}(b) = \frac{2}{c^2} \int_{-\infty}^{+\infty} \vec{\nabla}_\perp \phi dz \quad (1.19)$$

If the lens is a point mass (as shown in fig. 1.1)

$$\Phi = -\frac{GM}{r} \quad (1.20)$$

with $r = \sqrt{x^2 + y^2 + z^2} = \sqrt{b^2 + z^2}$ and $b = \sqrt{x^2 + y^2}$. The deflection angle then comes out to be

$$\hat{\alpha}(b) = \frac{2GM}{c^2} \int_{-\infty}^{+\infty} \frac{dz}{(b^2 + z^2)^{3/2}} = \frac{4GM}{c^2 b} \hat{b} \quad (1.21)$$

1.3 Lens Equation

The point mass or cluster of objects form a lens which causes the bending of light from a source on its way to an observer. To make our calculations easier, we can assume that the source and the lens can be replaced by planes with projected mass density.

This thin screen approximation works because light travels huge distances in the cosmological context where the lens systems can be seen as perturbations in an otherwise smooth, undeflected path; also, the maximum deflection occurs near the point of nearest contact of the light path with the lens.

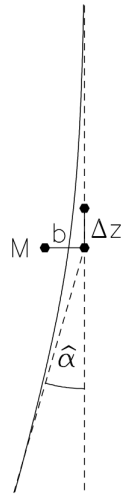


Figure 1.1: Deflection of light path by angle α due to a point mass M with impact parameter b .

Consider such a source-lens system as shown in fig. 1.2.
Using the angular diameter distance definition i.e.

$$\text{separation} = \text{angle} \times \text{distance} \quad (1.22)$$

we can write $\vec{\eta} = \vec{\beta}D_s$, $\vec{\xi} = \vec{\theta}D_d$ and $\theta D_s = \beta D_s + \hat{\alpha}D_{ds}$.
Defining the reduced deflection angle

$$\vec{\alpha} = \frac{D_{ds}}{D_s} \hat{\alpha} \quad (1.23)$$

we get the lens equation

$$\vec{\beta} = \vec{\theta} - \vec{\alpha}(\vec{\theta}) \quad (1.24)$$

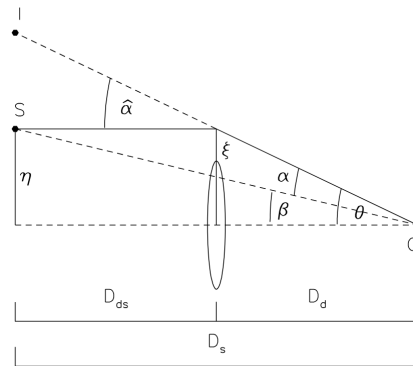


Figure 1.2: A source-lens system showing the deflection of light from a source S by a lens with impact parameter ξ on its way to an observer.

1.4 Gravitational Microlensing

Microlensing refers to a specific type of gravitational lensing caused by smaller objects like stars, planets or other massive compact objects.

When a distant star or quasar passes through the Einstein radius of a massive compact foreground object, its light bends around the lens which leads to two virtual images of the source, resulting in an **observable magnification**. The time-scale of the transient brightening depends on the mass of the foreground object as well as on the relative proper motion between the background ‘source’ and the foreground ‘lens’ object.

Microlensing was first observed in the multiply-imaged QSO 2237+0305 (Irwin et al. 1989). Paczynski in 1986 had the brilliant idea of using microlensing to search for DM candidates, the so-called Massive Astrophysical Compact Halo Objects (MACHOs) in the Milky Way halo.

1.4.1 Imaging a Point Source by a Point Mass Lens

For a point mass lens, we can use the Einstein radius to rewrite the lens equation in the form:

$$\beta = \theta - \frac{\theta_E^2}{\theta} \quad (1.25)$$

The lens equation has two solutions:

$$\theta_{\pm} = \frac{1}{2} \left(\beta \pm \sqrt{\beta^2 + 4\theta_E^2} \right) \quad (1.26)$$

Any source is imaged twice by a point mass lens. The two images are on either side of the source, with one image inside the Einstein ring and the other outside.

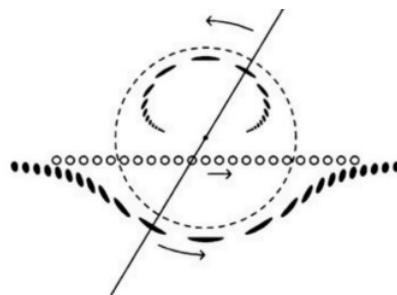


Figure 1.3: The movement of the two images in a Microlensing event

1.4.2 Magnification

Gravitational lensing preserves surface brightness of source, but changes the apparent solid angle of a source. Thus the total flux received from source increases and so does its apparent magnitude. For a circularly symmetric lens, the magnification factor μ is given by

$$\mu = \frac{\theta}{\beta} \frac{d\theta}{d\beta}, \quad (1.27)$$

$$\mu_{\pm} = \left[1 - \left(\frac{\theta_E}{\theta_{\pm}} \right)^4 \right]^{-1} = \frac{u^2 + 2}{2u\sqrt{u^2 + 4}} \pm \frac{1}{2} \quad (1.28)$$

In general for a Lens $\sim M_{\odot}$, the angular separation of the two images is too small to be resolved. However, even when it is not possible to see the multiple images, the time variable magnification can still be detected if the lens and source move relative to each other.

1.4.3 Light Curve

The expected time scale for microlensing-induced variations is given in terms of the typical angular scale θ_E , the relative velocity v between source and lens, and the distance D_d to the lens:

$$t_0 = \frac{D_d \cdot \theta_E}{v} \quad (1.29)$$

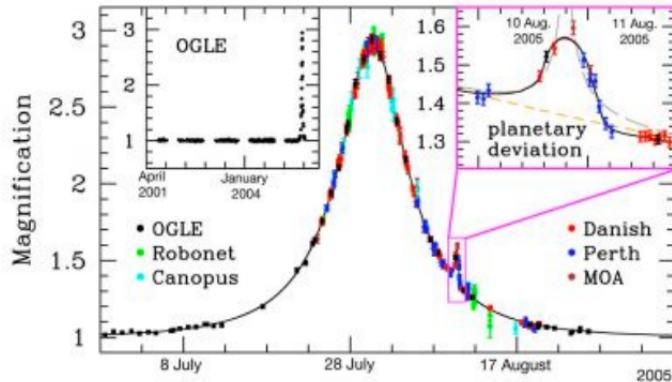


Figure 1.4: A Microlensing-induced light curve for a star-star event, also a possible exoplanet-star event can be seen.

Depending on the distance of closest separation between source and lens, we get a characteristic light curve for magnification of the source.

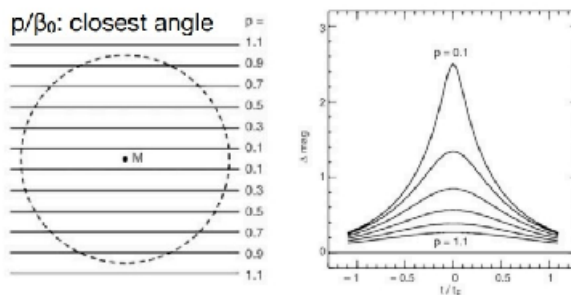


Figure 1.5: Microlensing-induced light curves for different separations between the source and the lens p . The separation is expressed in units of the Einstein radius.

1.5 Microlensing Simulation 1

A Python simulation of microlensing events was made for a fixed point lens object and a moving point source behind the lensing plane, with the following parameters: the Lens Position, R_E value and Impact parameter(Distance of closest approach) scaled by R_E .

The Simulation then animated the two images of the source and plotted the light curve for the event in real-time.

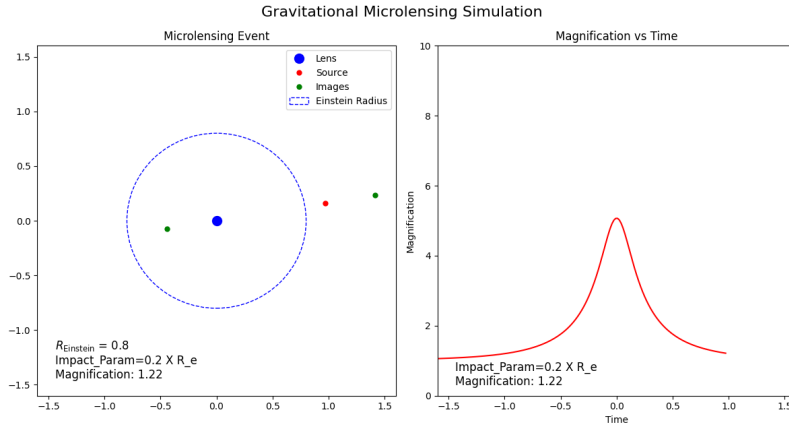


Figure 1.6: A single frame from the Simulation Output Display

Microlensing Event at $R_E = 0.8$, Impact_Param = $0.2 \times R_E$

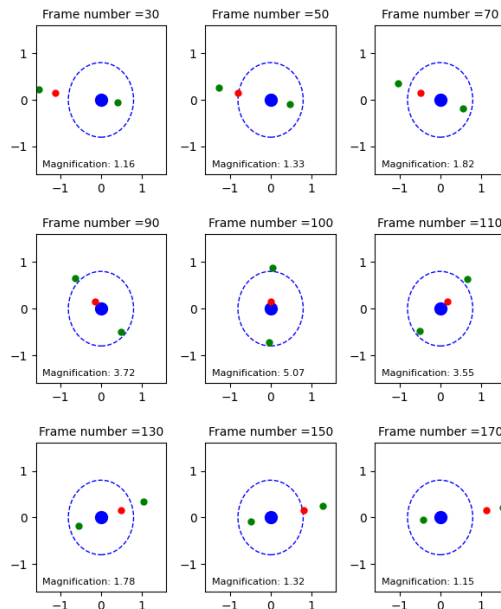


Figure 1.7: Frames depicting movement of the images, as the source passes through the Einstein tube of the lens.

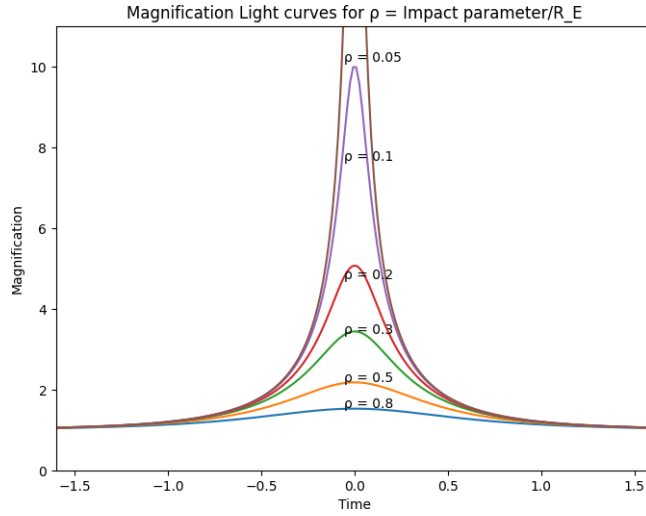


Figure 1.8: Observed light curves for varying closest separation distances between source and lens (impact parameter)

1.6 Microlensing Simulation 2

Another Python simulation of microlensing events for a fixed point source and a lens moving across the source line of sight. This is a more realistic microlensing simulation with free parameters: M_{lens} , D_l , D_s , D_{ls} (These give the value of R_E for the lens); b -impact parameter; and V_t -Tangential Velocity of the lens relative to the source in the lensing plane.

The animation output gives the magnification measured by a detector (light-curve) but not the images.

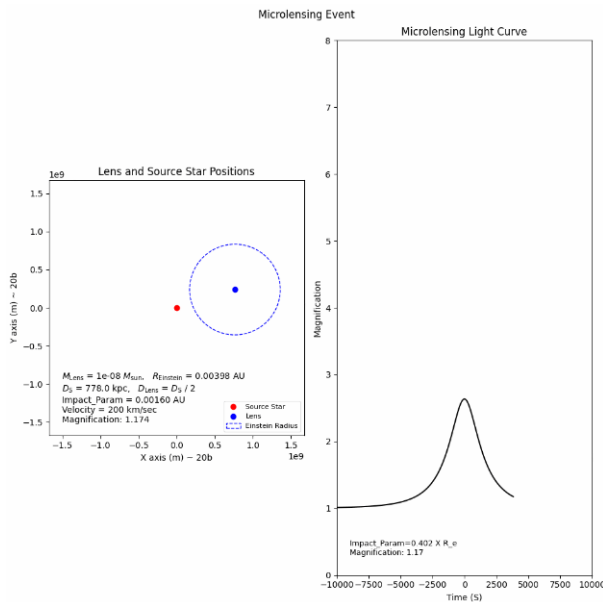


Figure 1.9: A single frame from the Simulation Output Display. Note the fixed source and moving lens.

We used the following standard parameter values for microlensing of an Andromeda star by an axion minicluster in Milky Way Halo.

$$\begin{aligned}
 M_{lens} &= 10^{-8} M_{\text{sun}} \\
 V_t &= 200 \text{ km/sec (Tangential velocity)} \\
 b &= 1.6 \times 10^{-3} \text{ AU (Impact parameter)} \\
 D_S &= 778 \text{ kpc (Distance to source - Andromeda)} \\
 D_L &= D_S / 2 \text{ (Distance to lens)} \\
 D_{LS} &= D_S - D_L \text{ (Distance between lens and source)}
 \end{aligned}$$

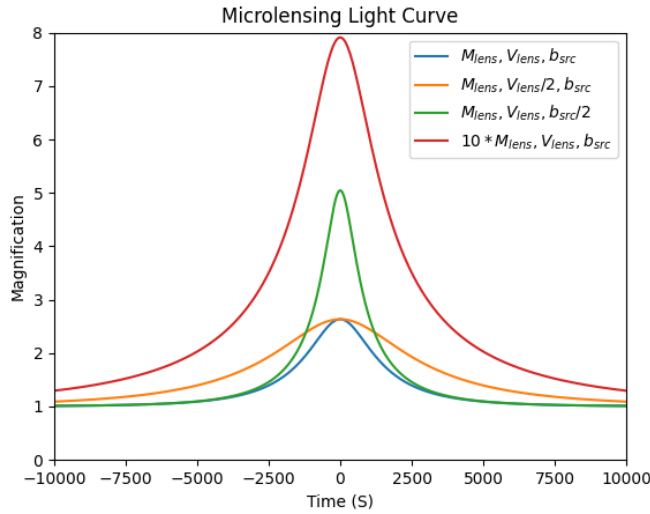


Figure 1.10: Observed light curves for varying the free parameters: M_{lens} , V_{lens} , b



2. Dark Matter Candidates

2.1 Introduction

2.1.1 What do we know about dark matter ?

author: Mehul Goyal

- Expressed as a fraction of the total density of the universe, Dark Matter makes up 26 percent of the universe, compared to 6 percent in ordinary matter and 68 percent in dark energy. The strongest evidence for this distribution comes from the anisotropies in the Cosmic Microwave Background. Cosmic Microwave Background is composed of the photons that decoupled from baryons after the recombination. The fact that baryons were tightly coupled to the photons before the recombination, while dark matter was not, allowed us to compute the densities of matter and dark matter separately from the Cosmic Microwave Background
- The local density of dark Matter is around 0.3 to 0.4 GeV cm $^{-3}$, which equivalent to one proton every few cubic centimeters or one solar mass per cubic light year. The actual density at precise location of the Earth can be different. This is particularly relevant to axions as they can also form mini clusters as discussed later.
- The velocity dispersion of Dark Matter is around $v = 200$ km s $^{-1}$, and our local motion with respect to the galactic rest frame is towards the constellation Cygnus.
- Dark Matter must be non relativistic and have negligible pressure. Galaxy formation would not be possible in case of relativistic dark matter
- Dark Matter had to be present, as well have a gravitational influence in the Universe long before the Cosmic Microwave background formed, and its gravitational influence began before the universe was 1 years old.
- Dark Matter is weakly interacting. It cannot interact with itself or ordinary matter too strongly.

2.2 QCD Axion

author: Mehul Goyal

2.2.1 The Standard Model

The Standard Model is a mathematically consistent quantum field theory whose predictions have been experimentally verified to an astounding precision. The Standard Model provides a very accurate description of all the visible matter in the universe, quarks and leptons, the electromagnetic, weak and strong nuclear forces acting between them. The crowning success of the standard model was the

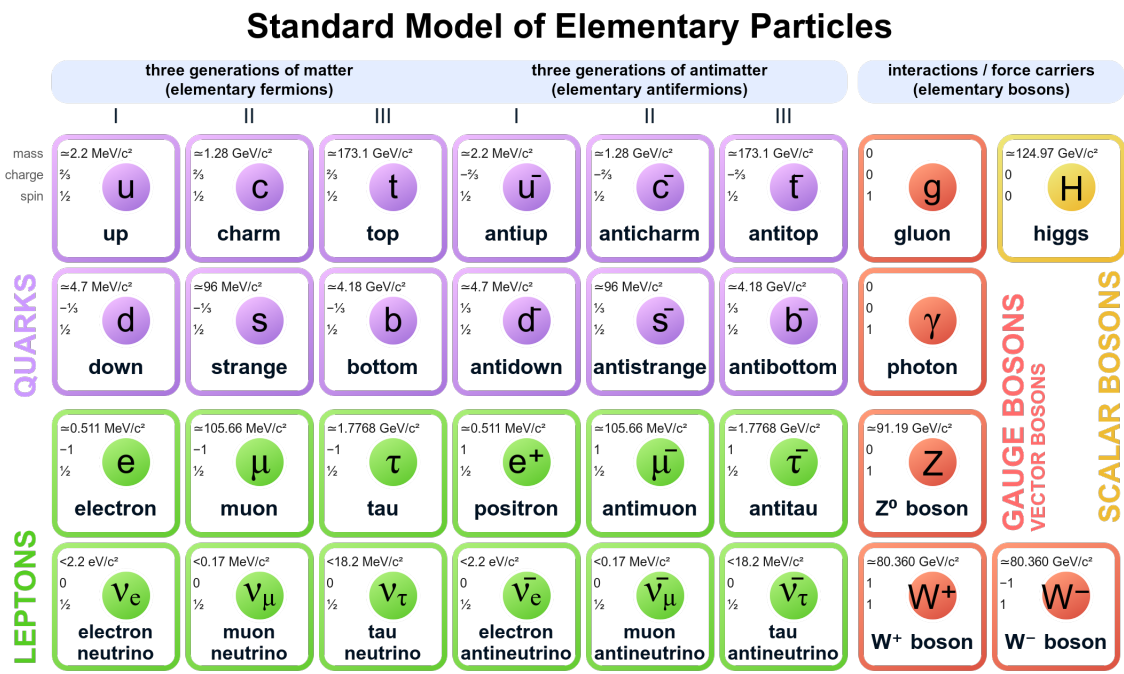


Figure 2.1: The Standard Model

discovery of the Higgs Boson. We will discuss the Higgs Mechanism shortly. Some predictions of the standard model which have been verified by experiments to astounding precision include existence and mass of top quark and gyromagnetic ratio of electron to name a few.

Despite the manifold successes, the standard model has left theoretical physicists unsatisfied due to its various shortcomings. We will discuss the two major shortcomings which are addressed by the theory of axions. The term "axion" for the particle arising from the solution to the strong CP problem described below, are also known as the QCD Axions. There are other theories for Dark Matter particles described by ALPs (Axion Like Particles), which can be very different from the QCD Axion discussed here.

- The Standard Model predicts existence of antiparticle of every particle. However, astrophysical and cosmological observations tell us that most of the visible matter that we see today is composed of matter and no large con-

centrations of antimatter have been found. This is called the cosmological matter-antimatter asymmetry.

- Theory predicts CP symmetry violation in case of the weak force, which was observed experimentally in 1957 by Chien-Shiung Wu. Quantum Chromodynamics, the quantum field theory for the strong force, in theory allows for CP violations in case of the strong force as well. CP Violation in case of the strong force has not been seen experimentally and this called the Strong CP problem. One of the consequences of CP Violation in case of strong force is non-zero electric dipole moment of the neutron.

2.2.2 CPT Symmetry

Charge (C), Parity (P) and Time Reversal(T) symmetry is a fundamental symmetry of physical laws under the simultaneous transformations of charge conjugation, parity transformation and time reversal. CPT is the only combination of charge, parity and time that is observed to be an exact symmetry of nature at the fundamental level.

The CPT Theorem says that the CPT Symmetry holds for all physical phenomenon, or more precisely, that any Lorentz Invariant local quantum field theory with a Hermitian Hamiltonian must have the CPT Symmetry. In order to preserve this symmetry, every violation of the combined symmetry of two of its components (such as CP) must have a corresponding violation in the third component (such as T). Thus violations in T-Symmetry are often referred to as CP violations

Electric Dipole Moment of Neutron

If the strong force is CP violating, it is predicted that the neutron will exhibit an electric dipole moment. The neutron electric dipole moment will violate the CPT symmetry. As we discussed above, if something violates CP symmetry, in order for the CPT symmetry to hold, there must be a corresponding violation in T. As an illustration, we will discuss this in case of electric dipole moment of neutron. If the

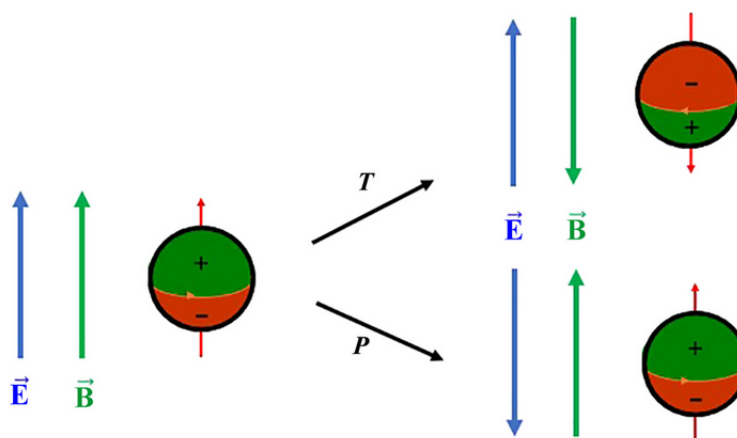


Figure 2.2: The effect of transformations of time reversal and parity on electric dipole

neutron has an electric dipole moment, by Wigner Eckart Theorem we know that it must be aligned with the neutron's spin (All the other components of EDM will be averaged to zero). As shown in the diagram above, if we reverse the direction of

time, the direction of neutron's spin will also get reversed. Therefore, the direction of electric dipole moment of neutron will change under a T transformation. However, the direction of electric field remains the same under a T transformation. Therefore, the energy of neutron in an electric field will change under a T transformation, violating the T symmetry and as a consequence the CP symmetry as well. Note how the EDM of neutron will violate P symmetry as well, as illustrated through the above figure.

2.2.3 Spontaneous Symmetry Breaking and Higgs Mechanism

Spontaneous Symmetry Breaking can describe systems where the equations of motion or the Lagrangian obey symmetries, but the lowest energy vacuum solutions do not exhibit the same symmetry. The discovery of the Higgs Boson in 2012 proved the existence of an elementary spin zero boson undergoing spontaneous symmetry breaking. This proof of principle invalidated the theoretical prejudice against the QCD Axion, which shares these properties with the Higgs Boson.

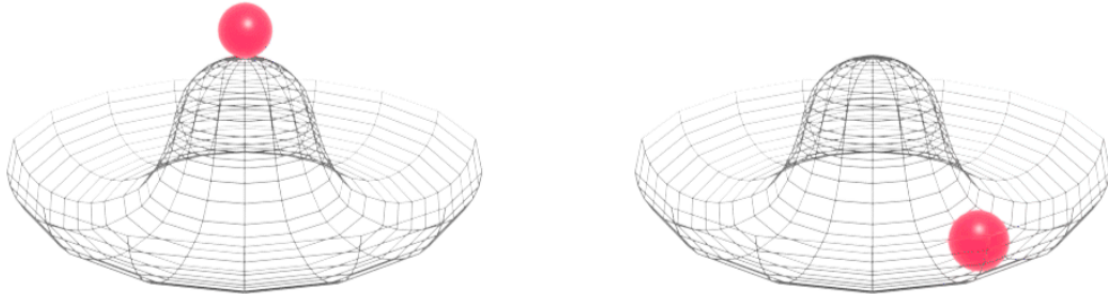


Figure 2.3: Particle in 'Mexican Hat' potential showing spontaneous symmetry breaking

Quantum Field Theory successfully explained electromagnetic interaction through quantum electrodynamics. Quantum electrodynamics is an abelian gauge theory with U(1) symmetry group and has one gauge field, the electromagnetic four potential, with the gauge boson being the photon. The success of Quantum Electrodynamics in explaining the electromagnetic interaction motivated physicists to apply the same approach to explain the weak interaction. But the approach faced a major challenge in explaining the weak interaction. The Gauge Bosons were required to be massless in order to protect the symmetries of the theory, which was in direct conflict with the need for massive weak force carriers (W and Z bosons). The weak force carriers needed to be massive to explain the short range of the weak force.

The solution came through the Brout-Englert-Higgs mechanism, which introduced a new quantum field, the Higgs field, and the process of Spontaneous Symmetry Breaking. An analogy for spontaneous symmetry breaking is a pencil standing on its tip. Initially, the system is symmetrical, but as soon as the pencil falls, it breaks the symmetry by selecting a direction, though the fundamental laws remain unchanged. We can also try to understand the process through a sombrero potential system as shown in the above figure. Imagine a ball initially at the top of the peak of the potential. In this initial metastable state, the system is completely symmetric. But due to quantum fluctuations, the ball can spontaneously roll down

in an arbitrary direction to a stable state, which no longer has the symmetry of the initial system, even though the equations still possess the original symmetry.

The way this worked for particle masses is as follows: In the early universe, the Higgs field was in a symmetrical but unstable state. Shortly after the Big Bang, the Higgs field transitioned to a stable state that broke the initial symmetry. This broken symmetry allowed the W and Z bosons to acquire mass while preserving the overall symmetry of the equations.

2.2.4 Peccei-Quinn Symmetry

Peccei-Quinn symmetry is a global axial U(1) symmetry.

A global symmetry is one that keeps a property invariant for a transformation that is applied simultaneously at all points of spacetime, while a local symmetry is one with a different symmetry transformation at different points of the spacetime, that is, a local symmetry transformation is parameterized by the spacetime coordinates. Axial means that symmetry transformations act differently on left and right handed particles. Right handed particles have their velocity aligned with the orientation of spin while left handed particles have their velocity opposite to the spin orientation. U(1) is equivalent to symmetry in rotation about an axis.

2.2.5 Nambu-Goldstone Bosons

Nambu-Goldstone bosons are bosons that appear necessarily in models exhibiting spontaneous breakdown in continuous symmetries. Let's consider an example of spontaneous symmetry breaking in case of magnets. Imagine a number of magnets at a very high temperature, which makes them move randomly. As the system cools down, this random thermal motion gets overpowered by the magnetic interaction and they all end up aligning in an arbitrary direction. The equations do not start out with a preferred direction, but under certain conditions the system chooses a preferred direction. In this case, the goldstone bosons are called *magnons*.

When you write down the Lagrangian in Quantum Chromodynamics, the CP violating terms are characterized by a parameter θ , which is known to be an angle and can take any value between 0 and 2π . Symmetry specifies no preferred value. The value of θ is what determines the electric dipole moment of the neutron. Peccei and Quinn proposed θ to be a dynamical quantity over both space and time, i.e. they proposed θ to be a new quantum field for which the value $\theta = 0$ is energetically favourable. This provides a natural way to preserve CP symmetry in strong interactions. The Nambu-Goldstone boson of PQ Symmetry is the axion and the quantum field associated with it is the θ field.

2.2.6 QCD Cross Over

We haven't solved the strong CP problem yet, as the axion field can apriori take any value due to the degeneracy in the lowest energy solutions of Sombrero Potential. The next part of the story is QCD Cross Over.

In the early universe, the temperature had to fall below a certain temperature for the protons and neutrons to exist. Below this temperature (≈ 200 MeV), QCD becomes strongly coupled and confines quarks and gluons (the carriers of strong force) into bound state protons and neutrons. This cross-over breaks the PQ symmetry and distorts the sombrero potential as shown in the above figure, resulting

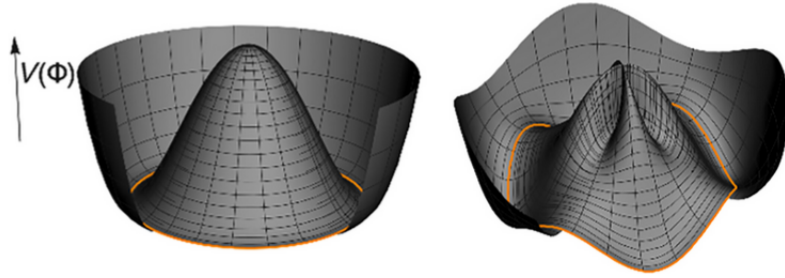


Figure 2.4: Sombrero Potential of PQ Symmetry

in a discrete minima. Thus, after the QCD Cross Over, the axion field rolls down to the value of one of these minima and the CP violating terms in QCD Lagrangian vanish.

2.2.7 Axion Dark Matter

The QCD Axion is one of the most viable candidates for dark matter particles. The axion is a pseudo Nambu-Goldstone boson of the spontaneously broken Peccei Quinn symmetry. We call it ‘pseudo’ because the PQ symmetry not being an exact symmetry, is explicitly as well as spontaneously broken. The explicit breaking results in Axions not being massless like the goldstone bosons are required to be, but are still extremely light particles ($\approx 10^{-5}$ ev).

The cosmology of the axion dark matter depends upon the epoch of cosmology during which the PQ symmetry is broken. If the symmetry gets broken during the inflationary period, all the complexity of the phase transition is lost. This is because epoch of inflations smooths the universe (consequently the axion field) on the largest of scales, in accordance with the observations. In this case, the evolution of axion dark matter is described by a wave equation with the expansion of the universe acting as a damping term. The two inputs to the wave equation are the initial value of the axion field and the axion mass.

The alternate scenario is that the PQ symmetry breaks after the smooth cosmic initial conditions have already been established by the inflation epoch. In this case, the axion field is not smoothed out and has topological defects. There are large amplitude axion field fluctuations present on the scale of hubble horizon at that time. The Kibble mechanism smoothes the axion field on scale of the horizon till the time when expansion rate of the universe falls below the natural frequency of oscillation of the axion field, which is dependent on the mass of the axion ($3H(t_0) \approx m_a$, where H is the Hubble rate). From this point onwards, the axion field oscillates about minima, and its equation of state becomes that of pressureless matter. It is at this time that axions are produced in large numbers. This epoch last for a short period, as the large-scale energy density of the axion field, stored up from the phase transition, is converted into axion particles. Post the production epoch, the axions “freeze-out” and their co-moving density becomes constant, this means that number density of axions is diluted away by the expansion of the universe. The number density of a particle at the time of its freeze-out is called its relic density.

In the latter scenario, there is possibility of formation of axion minicusters which shall be discussed later. Due to large de Broglie wavelength of axions (owing to their extremely low mass and non-relativistic nature), axions populate the universe in a

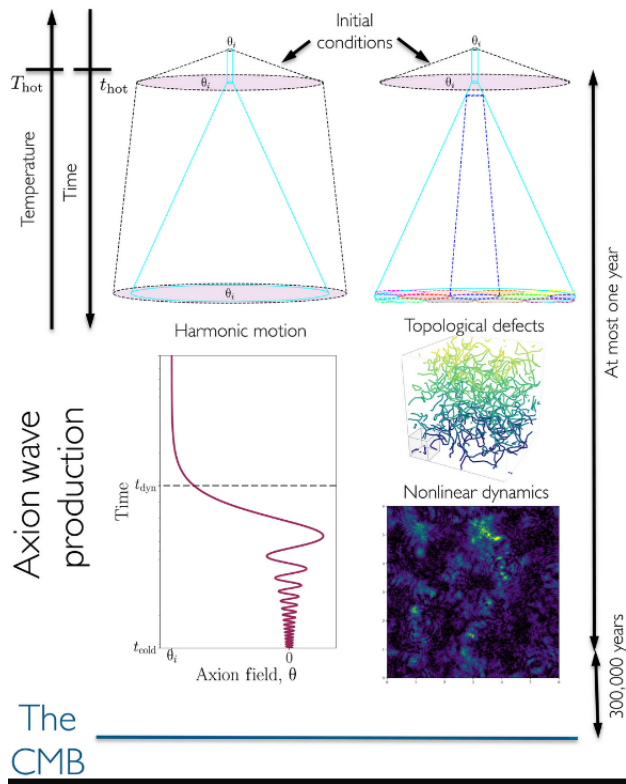


Figure 2.5: Alternate scenarios of axion DM evolution depending on the epoch in which PQ symmetry breaks. The scenario in which PQ symmetry breaks during inflation is on left and post inflation scenario is on the right. t_{Hot} is the time at which inflation ends, t_{dyn} is the time at which axion production starts, t_{cold} is the time at which axions "freeze-out"

coherent wave like state.

Some of the characteristic features of axion DM that separate it from its heavier counterparts like WIMP are :

- The de Broglie Wavelength. Gradient Energy dominates over gravitational on smaller scales. As a consequence, the axion field is smooth on small scales and there is a minimum mass for Dark Matter halos.
- At very high densities, the axions can potentially form an axion star. At these extreme densities, axions can form a soliton (a stable wave-like configuration) supported b an equilibrium between gravity and gradients.
- Wave Turbulence and interference. In the structures of cosmic web, axion waves have dynamical velocities. Where there are coherent flows, this leads to interference patterns in filaments

A visual depiction of these unique features is present in the following figure.

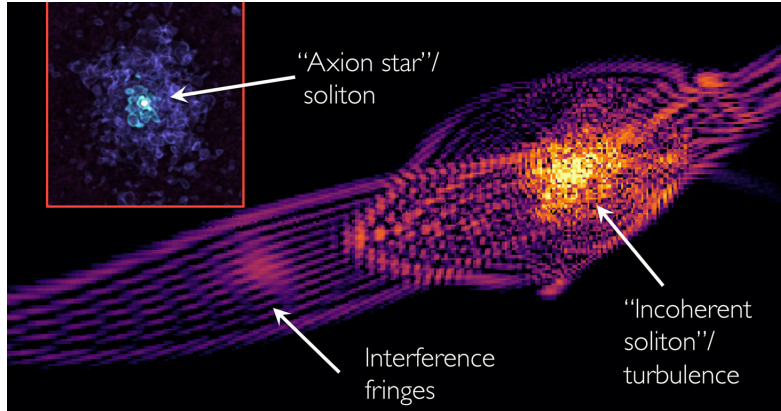


Figure 2.6: Parts of cosmic web formed by gravitational interactions and interference of axion waves

2.3 Primordial Black Holes

author: Chirag Sharma

As the name suggests, Primordial black holes (PBH) are black holes that formed in the early universe, just after the end of the inflationary period.

These are formed by the collapse of density perturbations in the radiation domination era.

The reason PBHs are considered as a candidate of dark matter is that they fulfill all of the basic criteria of being dark matter. PBHs are cold i.e. non-relativistic, and as they formed in the early universe i.e. before the big bang nucleosynthesis, they are non-baryonic and they are stable (see 2.3.1).

PBHs are one of the unique dark matter (DM) candidates as they do not bring any new particles with them in the DM modeling, unlike most other candidates.

Now, let's discuss about the formation of these primordial black holes.

2.3.1 Formation of PBH

For the formation of these black holes, we need a collapse of large-density perturbations. The standard slow-roll inflationary period does not give rise to perturbations this large. So, we need a brief period of ultra slow-roll to generate enough power for these density fluctuations.

For the scalar field ϕ driving inflation, the standard equation of motion is

$$\ddot{\phi} + 3H\dot{\phi} + V'(\phi) = 0 \quad (2.1)$$

For slow-roll inflation, $\ddot{\phi} \approx 0$, which implies we get the following as the equation of motion for the slow-roll inflation

$$3H\dot{\phi} + V'(\phi) = 0 \quad (2.2)$$

However, during ultra-slow-roll inflation, $V'(\phi) \approx 0$ which gives us

$$\ddot{\phi} + 3H\dot{\phi} = 0 \quad (2.3)$$

So the inflation period now consists of a brief ultra-slow-roll period, the usual slow-roll, and reheating at the end for the inflaton energy to decay into standard model

particles.

To form a PBH, you need large-density perturbations to collapse. During inflation, the horizon (aH) $^{-1}$) decreased while the universe faced exponential expansion. The density contrasts were stretched to macroscopic scales. As PBH formation is a causal process, a PBH cannot be formed during inflation when the different patches of the universe are not in causal contact. Only after the end of inflation, a mode can transfer its enhanced energy due to inflation, to density perturbations during radiation domination upon re-entry in the horizon. So, a PBH of scale $1/k$ cannot form while $k \ll aH$. This is depicted in fig. 2.7.

Assuming that PBH formation takes place by the collapse of density perturbations

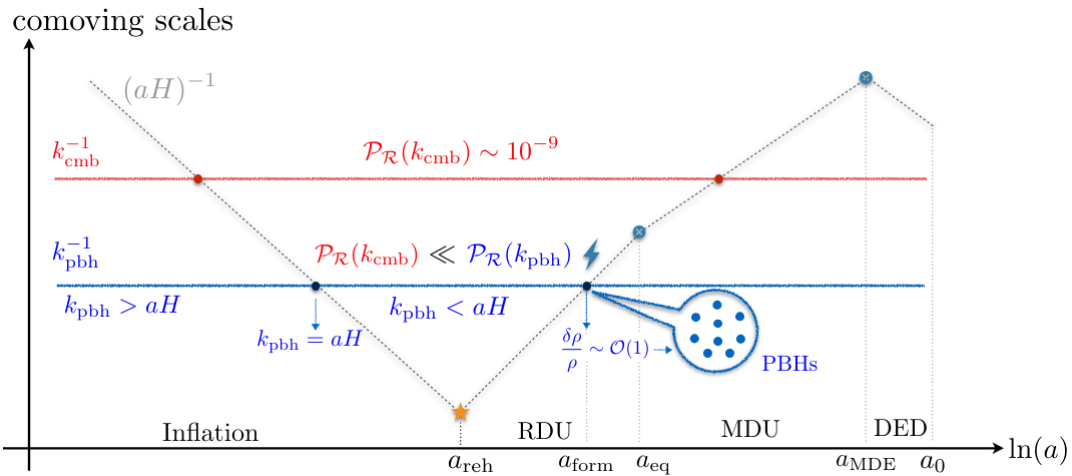


Figure 2.7: Evolution of comoving scales with the Hubble horizon $(aH)^{-1}$. The blue horizontal line denotes a perturbation mode which can be responsible for PBH formation. Plot from Ogan, Tasinato 2023

of a mode when it re-enters the horizon during radiation domination, we can find an upper limit on the mass of the PBH M_{PBH} .

We work with the FLRW metric

$$ds^2 = -dt^2 + a^2(t)(dr^2 + d\Omega_2) \quad (2.4)$$

where $d\Omega_2$ describes the line element for a 2-sphere. For photons, $ds = 0$ and Hubble radius $(aH)^{-1}$ is the radial distance,

$$\int_0^t \frac{dt}{a(t)} = \int dr = \frac{1}{aH} \quad (2.5)$$

$$\frac{1}{H} = a(t) \int_0^t \frac{dt'}{a(t')} \approx 2t \quad (2.6)$$

where for the last equality, we have used the relation $a \approx t^{1/2}$ during radiation domination.

Now,

$$M_{PBH} = M_{Horizon} = \rho V_{Horizon} \quad (2.7)$$

where ρ is the density and $V_{Horizon}$ is the volume of the horizon or the Hubble Volume at the time of the collapse of the Hubble Mass $M_{Horizon}$ which is during

the radiation domination era. To cause the mass to collapse, we use the critical density $\rho_{cr} = \frac{3H^2}{8\pi G}$ and the Hubble Volume is given by

$$V_{Horizon} = \frac{4}{3}\pi R_{Horizon}^3 \quad (2.8)$$

Using these values and eq. 2.6 in eq. 2.7, we get

$$M_{PBH} = \frac{tc^3}{G} \quad (2.9)$$

where we have inserted the speed of light factor c back into the equation. We can rewrite this equation as

$$M_{PBH} \approx 10^{15} g \frac{t}{10^{-23} s} \quad (2.10)$$

and this equation tells us that a PBH with mass $10^{15} g$ would be evaporating by Hawking radiation in the present epoch, while PBH of mass greater than this limit would be stable and thus, can account for dark matter.

2.3.2 Observing Signatures of PBH

We focus on a recent paper on studying PBH as dark matter candidates¹. Various constraints like accretion and dynamical processes, lensing probes, Hawking evaporation limit allows for PBH in the mass range $10^{-16} M_\odot - 10^{-11} M_\odot$ to account for 100% of the dark matter (see fig. 2.8).

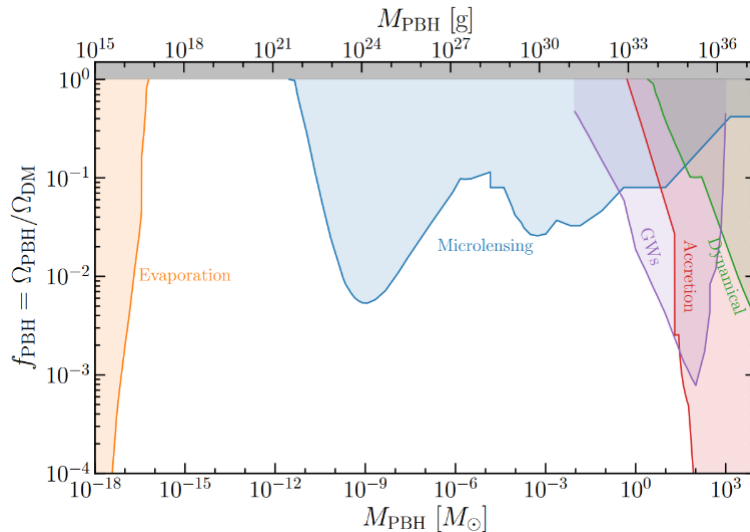


Figure 2.8: Plot from Marc Oncins, 2022. The shaded region represents the mass range excluded by various probes.

To probe PBH in this window, we need to make use of X-rays and more specifically, X-ray microlensing.

To find microlensing events from observational data of a pulsar, we follow a statistical approach as described in the paper (1).

¹ by Manish, Nirmal and Prateek of IISc Bangalore. arXiv:2405.20365

We download a segment of NICER observation data for a pulsar SMC-X1 using NASA data archive. We run the data analysis software HEASOFT and process the data with the `nicer-l2` pipeline to get a cleaned event file. Then, this is processed again with the `nicer-l3` pipeline to produce light curves. After doing these steps, we'll get a plot like fig. 2.9

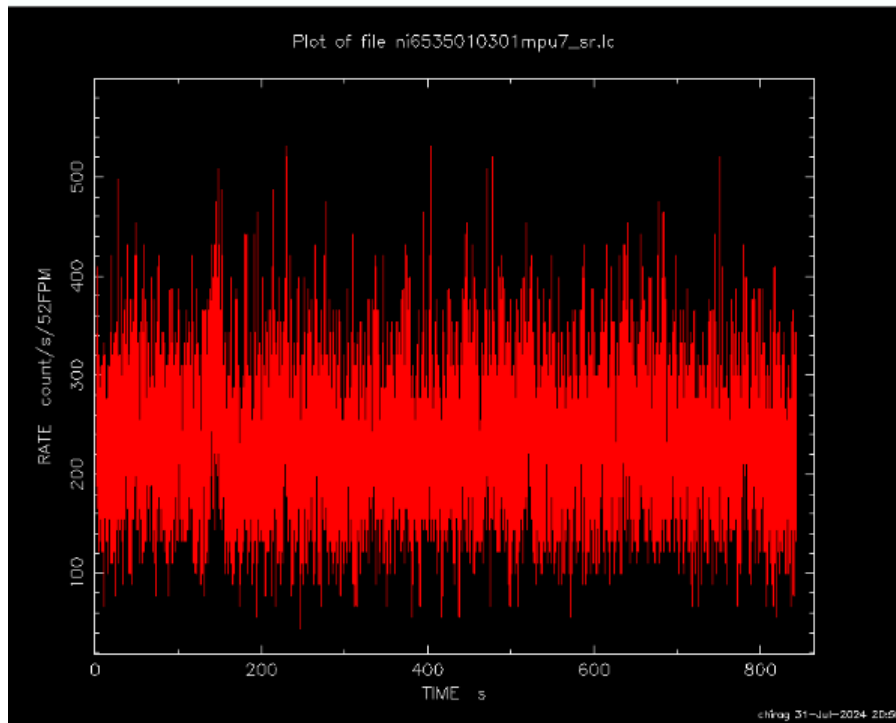


Figure 2.9: Light curve for a 864 second segment of SMC-X1 pulsar NICER data extracted using HEASOFT.

Then, we can do signal processing to remove the noise and get a scatter plot of the light curve. Following the statistical prescription, we'll say we found a microlensing event if we get 3 consecutive time bins which have photon counts larger than mean $+3\sigma$.

Microlensing by PBH in the geometric optics regime produces magnification which is independent of the source frequency. Using this fact, we can filter events like X-ray bursts and other events that can cause high photon counts. We can achieve this by observing the event in two different energy windows and classifying it as a microlensing event if the light curve is identical.

Following this, we can calculate decay rates, as described in the paper, to find limits on PBH in this mass range.

2.4 Weakly Interacting Massive Particles

author: Suryansh Srijan

2.4.1 What exactly are Weakly Interacting Massive particles?

Weakly Interacting Massive Particles (WIMPs) represents a lot of hypothetical candidates. Generally, this includes any non-baryonic massive particle that interacts with any weak or sub-weak interaction (e.g., axionic, gravitational). In the case of WIMPs, self-interactions are also weak. The most popular WIMP candidate is the lightest neutralino of supersymmetry (SUSY). To explain the relic abundance of DM as WIMPs, the freeze-out mechanism is used.

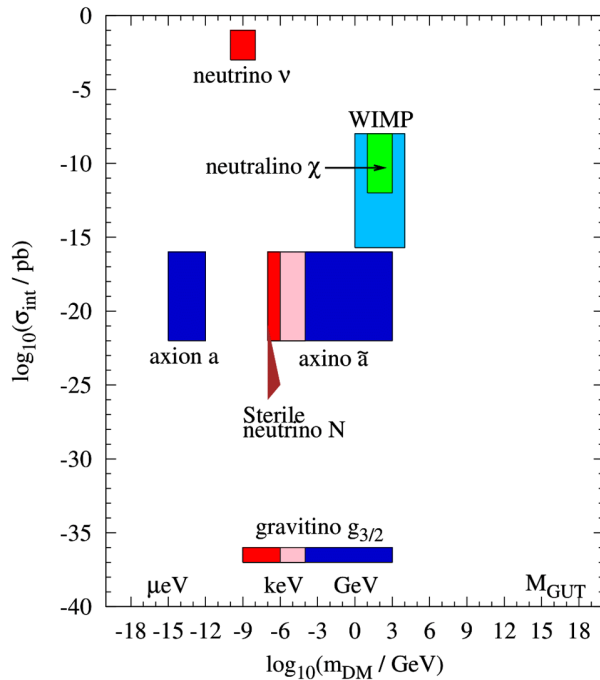


Figure 2.10: Typical ranges of the cross-section of DM interactions with the ordinary matter as a function of DM mass are shown for some DM candidates that are strongly motivated by particle physics. The red, pink and blue colours represent HDM, WDM and CDM, respectively.

2.4.2 Freeze-out Mechanism

In the early universe, WIMPs were in equilibrium with the rest of the cosmic plasma at high temperatures but then experienced a freeze-out when the temperature dropped below its mass. In the case of WIMPs, two heavy particles X can annihilate, and produce two light (essentially massless) particles. These lighter particles are assumed to be in complete equilibrium with the cosmic plasma. The Boltzmann equation for WIMPs thus obtained is:

$$\frac{dn_X}{dt} + 3Hn_X = -\langle \sigma v \rangle (n_X^2 - n_{X,\text{eq}}^2) \quad (2.11)$$

where H is the Hubble parameter, n_X is the number density, $n_{X,\text{eq}}$ is the equilibrium number density, and $\langle \sigma v \rangle$ is the mean annihilation cross-section times Moller velocity.

Rearranging the terms we get:

$$\frac{dn_X}{dt} = -3Hn_X - \langle\sigma v\rangle(n_X^2 - n_{X,\text{eq}}^2) \quad (2.12)$$

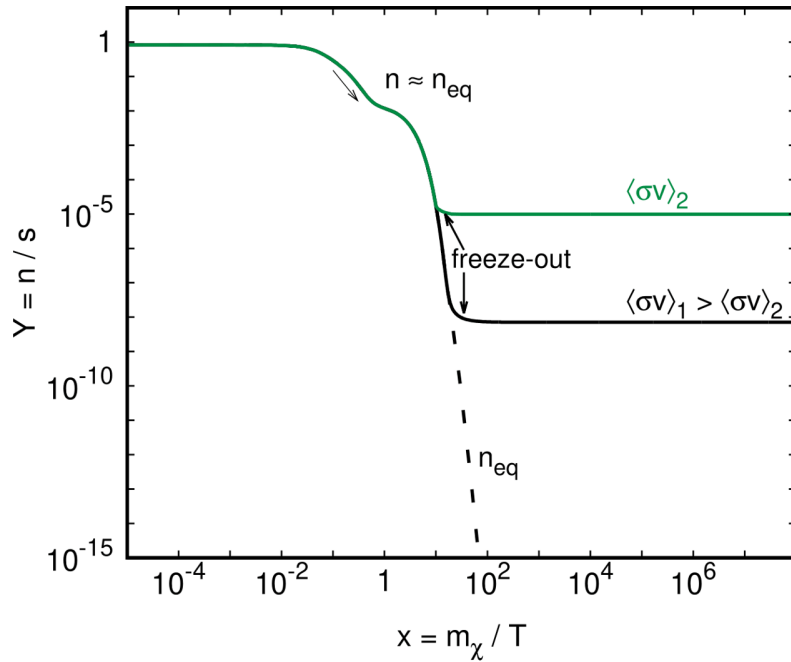


Figure 2.11: Evolution of the DM yield for a standard freeze-out scenario

2.4.3 WIMP Miracle

On carefully solving the Boltzmann equation, we get the following result:

$$\Omega_{\text{DM}} h^2 \approx \frac{3 \times 10^{-27} \text{cm}^3 \text{s}^{-1}}{\langle\sigma v\rangle} \quad (2.13)$$

Putting in a typical value of $v = 0.1c$, in thus obtained $\langle\sigma v\rangle$, gives an annihilation cross-section similar to that of weak forces. This coincidence is termed the WIMP miracle which made it an outstanding candidate for Dark Matter.

2.4.4 Supersymmetry

Supersymmetry is a principle used to extend the Standard Model. It provides elegant solutions to many current problems in particle physics. The Minimal Supersymmetric Standard Model (MSSM) is the simplest extension of the Standard Model that resolves many conflicts in the current Standard Model. MSSM proposes that a partner particle with different spin properties exists for every known particle. It provides two DM candidates: sneutrino (the superpartner of the neutrino) and the neutralino (a linear combination of two higgsinos, the wino, and the bino). The sneutrino has been ruled out due to its full-strength gauge couplings to SM and bounds from direct detection experiments.

2.4.5 Lightest Neutralino of SUSY

The neutralino is the lightest neutralino of supersymmetry and is the most promising DM candidate of SUSY. In most models, the LSP (lightest supersymmetric particle) is mostly Bino with some mixture of Wino and Higgsinos. Currently, there are many collider searches for supersymmetric particles, but none have been found. The lower bounds on the mass of all supersymmetric particles are increasing, but the LSP remains a viable DM candidate.

2.4.6 Experimental Situation

There are three ways to detect DM:

1. Direct Detection
2. Collider Searches
3. Indirect Detection

Motivation for Indirect Searches

Despite many model-dependent factors, most of them predict $\langle \sigma_{ann} v \rangle \sim 2 \cdot 10^{-26} \text{ cm}^3 \text{s}^{-1}$. Indirect searches that are sensitive to dark matter annihilating at approximately this rate, will be able to test a lot of WIMP models. E.g. a lot of gamma-ray searches, as well as cosmic-ray antiproton and positron, are sensitive to DM with predicted annihilation cross-section, for masses up to $O(100)\text{GeV}$.

2.4.7 Direct Detection

During DM annihilations, the residue lighter particles formed are assumed mostly to be gamma rays (or they further decompose to give gamma rays). Most direct detection approaches study gamma-ray signals. The brightest gamma-ray signal from DM annihilations is expected to come from the Galactic Centre (GC). The astrophysical background in the direction of the GC is difficult to model, but an excess of GeV-scale emission has been detected in the Fermi data. This gamma-ray excess is consistent with those expected from annihilating DM.

Another explanation for this gamma-ray excess is a large population of low-luminosity millisecond pulsars with few accompanying low-mass X-ray binaries. The arguments for and against these pulsars are currently in debate.

Dwarf Spheroidal Galaxies (dSphs)

dSphs in the Local Group do not suffer from the same problems as the GC of the Milky Way. dSphs are expected to be DM-dominated and are free from the astrophysical backgrounds plaguing the GC. The expected signal is much lower for a single dSph, therefore a stacking analysis is required.

Galaxy Clusters

Galaxy clusters are another promising target for gamma-ray searches. The main drawback compared to dSphs is that they suffer from large and poorly understood astrophysical backgrounds. The expected sensitivity depends strongly on the DM substructure, which is unknown.

2.5 Ultra Light Dark Matter

author: Akshank Tyagi

Ultra-light dark matter (ULDM) is a family of dark matter Candidates (DM) in which DM is composed of bosons with masses between $10^{-24} \text{ eV} < m < 1 \text{ eV}$ in the very vast mass range of all Dm Candidates (Fig 2.10).

These models have drawn a lot of interest in recent years because of their intriguing ability to generate Bose-Einstein condensates (BECs) or super-fluids on Galactic scales.

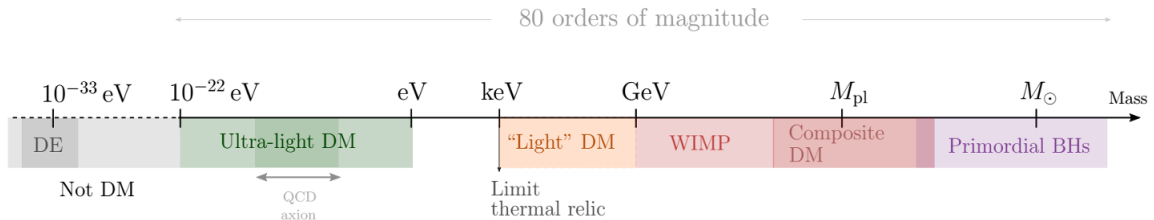


Figure 2.12: Sketch (not to scale) of the huge range of possible DM models that have been conceived

These Bosons upon condensation, act as a single coherent state, represented by the condensate's wavefunction. The concept is that condensation takes place within galaxies, while outside, on larger scales, it preserves the successes of Cold Dark Matter (CDM). This wave-like behavior of dark matter on galactic scales, emerging from condensation, can explain some of the peculiarities observed in DM behavior on smaller scales.

2.5.1 Discrepancies at Small Scales in Λ CDM

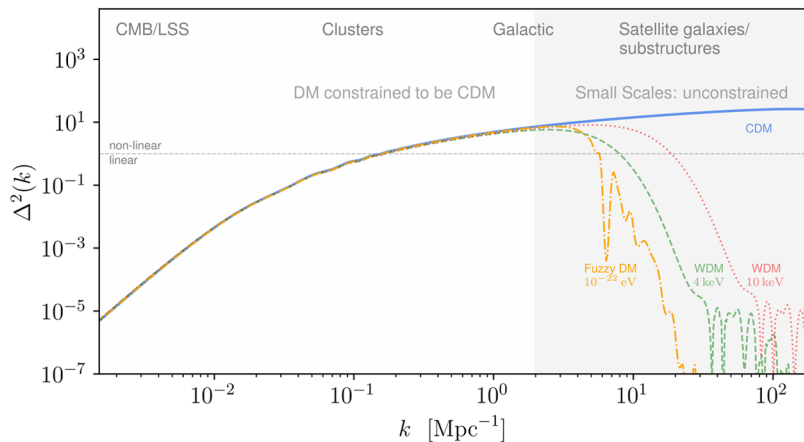


Figure 2.13: shows how the small scales might reveal different behavior for different DM components,

In this section, I will describe how some of the contentious theoretical predictions for DM halos from numerical simulations of the small scales considering the CDM model compares to astrophysical observations.

1. Cusp-Core Problem:

Expected density profile from collisionless simulations is the NFW(Navarro-Frank-White) cuspy profile at galactic Center:

$$\rho_{center} = 1/r^\gamma$$

$$\rho_{NFW}(r) = \frac{\rho_s}{(r/r_s)(1+r/r_s)^2} \rightarrow \begin{cases} 1/r, & \text{for } r \ll r_s \\ 1/r^3, & \text{for } r \gg r_s \end{cases}$$

NFW has $\gamma = -1$

THINGS and LITTLE THINGS measured Rotation curves of multiple dwarf galaxies and found smaller $\gamma = 0.29 \pm 0.07$

Solved by BEC Dark Matter and MOND theories

2. Missing Satellite Problem:

- DM Subhaloes- simulations predict several hundreds of subhalos with $v_{max} = 10 - 30$ kms, that are large enough to host a galaxy, around a Milky Way size galaxy

While till now SDSS and DES data shows 12 classical and around 40 Ultra faint Satellites for MW. Much less than predicted

Solution: One can expect that for low mass subhalos, galaxy formation is suppressed by striping gas mechanisms

- Massive DM Subhaloes- Most Massive subhalos predicted by those simulations have central masses ($V_{max} > 30$ kms) that are too large to host the observed satellite galaxies of MW which have ($12 < V_{max} < 25$ kms) which are not massive enough. The puzzle is why should the most massive subhaloes, where the gravitational potential is the strongest and the striping gas mechanisms cited above are not important, be too big to fail to form stars and galaxies?

Solution: BEC suppresses the formation of small scale subhaloes, and reduces the central densities of massive subhaloes (or modifies the dynamics of the central regions)

3. Scaling Relations:

- Baryonic Tully-Fischer Relation (BTFR) that relates the total baryon mass of the galaxy to the asymptotic circular velocity in galaxies,

$$V_f^4 = a_0 GM_b$$

This empirical scaling relation is shown to hold for large ranges of masses, almost 6 orders of magnitude the slope of the BTFR is different from the one predicted by CDM, $V_f^3 \propto M_b$

- Mass discrepancy Acceleration Relation (MDAR) : a relation between the gravitational acceleration from baryons alone and acceleration

inferred from rotation curves.

These empirical relations, coming directly from observations, show the surprising feature that in galaxies the dynamics is dictated by the baryon content, even when DM dominates. Even more unexpected these relations are very tight, showing very little spread, even if they come from very diverse types of galaxies

Solution: new high resolution simulations, like EAGLE, have been able to reproduce features of the rotation curves of galaxies within CDM include several baryonic effects (like star formation, stellar evolution, metal enrichment, gas cooling/heating, galactic outflows and BH feedback)

2.5.2 Bose-Einstein condensates and Super-fluids

Bose-Einstein condensation (BEC) occurs when a large fraction of bosons occupy the lowest energy state at extremely low temperatures, leading to the formation of a coherent macroscopic wavefunction that describes the entire system. This quantum mechanical phenomenon is marked by long-range coherence, where the wave nature of particles dominates, resulting in the condensation of bosons into a single quantum state.

Superfluidity, closely related to BEC, is a state of matter where a fluid flows without viscosity, allowing it to move frictionlessly. This behavior emerges when the quantum properties of particles lead to collective, coherent motion across the system.

In the context of ULDM, these concepts become crucial in understanding how dark matter might behave on Galactic/ sub-galactic scales. ULDM, composed of extremely light bosons, could form a BEC under certain conditions in the early universe, leading to large-scale coherence and unique astrophysical phenomena. If ULDM exhibits superfluidity, it could flow without resistance, impacting galaxy formation and dynamics, and offering an explanation for dark matter's elusive properties in a novel way. The interplay between BEC and superfluidity in ULDM models provides insights into the possible quantum nature of dark matter.

2.5.3 ULDM Model

The Upper bound is from the de Broglie wavelength of the ULDM particle is of the size of the galaxy This translates to the condition that de Broglie wavelength of the boson DM is larger than the inter-particle distance between each boson

$$\lambda_{dB} \sim \frac{1}{mv} > l = \left(\frac{m}{\rho}\right)^{1/3} \quad \Rightarrow \quad m < \left(\frac{\rho}{v^3}\right)^{1/4}$$

ULDM presents masses that are very small cannot be produced thermally in the early universe. Therefore, ULDM is a non-thermal relic of the Early Universe The QCD axions and axion like particles (ALPs) can have similar Properties to Fuzzy Dark matter

1. Fuzzy Dark Matter:

A gravitationally bounded scalar field model. In this model condensation under the influence of the gravitational potential is achieved in galaxies

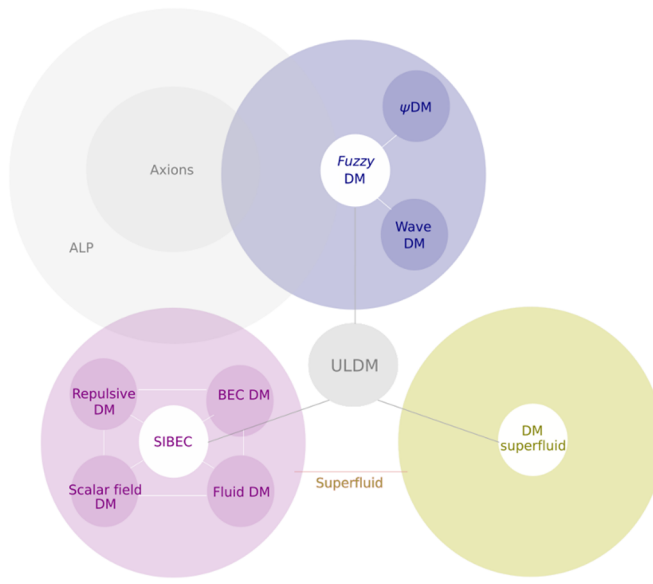


Figure 2.14: ULDM classes map

where the quantum pressure counteracts the gravitational attraction. One of its main candidates, where the DM is given by a light particle with $m = 10^{-22}$ eV. With a particle with this mass, the FDM model is known to be able to solve some of the challenges from small scales that we discussed, and to be in agreement with large scale observations. Forms gravitationally bounded BEC in Galactic halos and this model has only one free parameter, the mass of the FDM Particle.

2. Self-Interacting FDM:

A scalar field model, in the presence of gravity, with a 2-body self-interaction(or higher). The presence of these weak interactions makes this model present superfluidity upon condensation. This case is described by an interacting BEC.

The presence of the interaction controls the stability of the core and this this model presents a different phenomenology depending not only on the mass of the particle, as for FDM, but given the strength and sign of the interaction. This model has two free parameters.

For a repulsive interaction, the condensate has a long range coherence and presents superfluidity. The 2-body case is characterized by having an equation of state :

$$\text{EoS: } P \propto n^2$$

3. Dark Matter SuperFluid:

This was proposed with the goal of reproducing the MOND empirical law on small scales. Different than in the case of SIFDM, in order to reproduce MOND it requires that the equation of state is given by

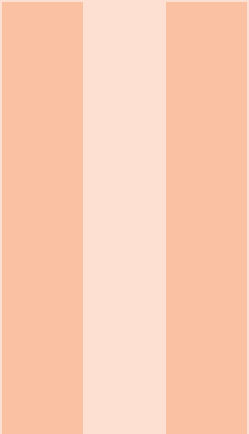
$$\text{EoS: } P \propto n^3$$

The model is described using the Effective Field Theory of Superfluids

Fuzzy DM vs SIFDM

$$\begin{cases} i\dot{\psi} = -\frac{1}{2m}\nabla^2\psi + m\Phi\psi + \frac{g}{8m^2}|\psi|^2\psi + \frac{g_3}{12m^3}|\psi|^4\psi + \dots \\ \nabla^2\Phi = 4\pi G(\rho - \bar{\rho}) \end{cases} \implies \begin{cases} g_i = 0 & \text{Fuzzy DM} \\ g_i \neq 0 & \text{SIFDM} \end{cases}$$

Figure 2.15: Gross–Pitaevskii equation for FDM and SIFDM, describes the evolution of a wavefunction or a field.



Part Two

3	Axion Miniclusters and their Microlensing signal	39
3.1	Evolution of Axion Field	
3.2	Axion Miniclusters	
3.3	Constraining Miniclusler Mass Function	
3.4	Miniclusler Density Functions	
3.5	Theroetical uncertainties in the MCH mass function and analytic results	
	Bibliography	49
	Articles	

3. Axion Miniclusters and their Microlensing signal

3.1 Evolution of Axion Field

Two energy scales define the cosmological evolution of the axion field: the decay constant, f_a , and the mass, m_a . Spontaneous symmetry breaking occurs when the universe's temperature cools to $T \leq f_a$. Breaking of the PQ symmetry following inflation might result in topological defects and huge amplitude axion field fluctuations on scales comparable to the horizon size.

Under smooth initial conditions, axion field evolution is governed by the Klein-Gordon Equation for a spatially homogeneous axion field $\phi_a(t)$:

$$\frac{d^2\phi}{dt^2} + 3H(t)\frac{d\phi}{dt} + m_a(T)^2\phi = 0 \quad (3.1)$$

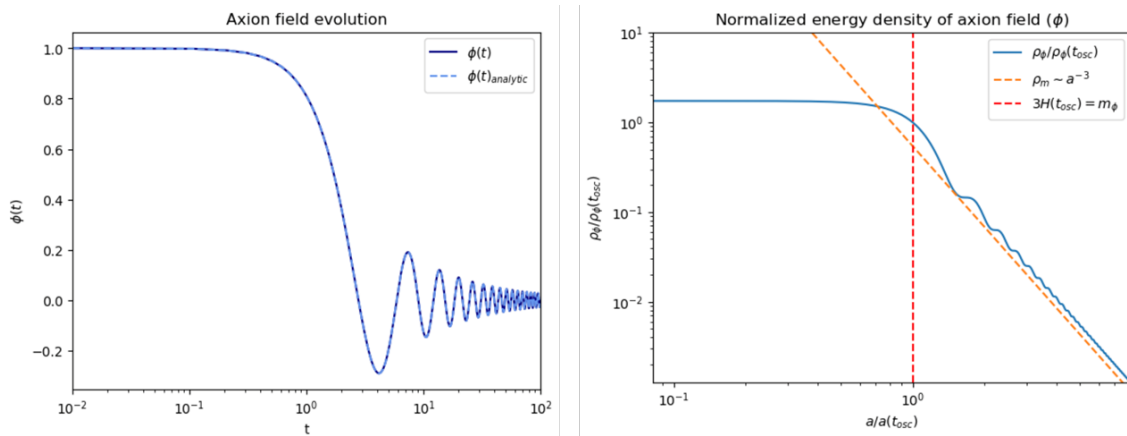


Figure 3.1: Evolution of the Axion Field (by Manish Tamta)

The next important epoch in the field evolution is when the Axion mass becomes cosmically relevant t_0 is (also sometimes called t_{osc} or T_{osc}), given by:

$$3H(t_0) \approx m_a(T). \quad (3.2)$$

The evolution of the axion mass is given by:

$$m_a(T > T_c) = m_{a,0} \left(\frac{T}{T_c} \right)^{-n}; \quad m_a(T < T_c) = m_{a,0} \equiv m_a. \quad (3.3)$$

The index n parameterizes the sharpness of the phase transition at temperature T_c , and $n \leq 6$ which comes from the lower bound on m_a . The QCD axion has a known temperature-dependent mass with $n = 3.34$ from the “interacting instanton liquid” model for the QCD topological susceptibility, which is consistent with the results from lattice simulations ($n \approx 3.55 \pm 0.30$).

The critical temperature $T_c \approx \sqrt{m_a f_a}$. For the QCD axion, $T_c \approx \Lambda_{\text{QCD}} \approx 200 \text{ MeV} \approx 2.5 \sqrt{m_a f_a}$. In the case $T_c \gg \sqrt{m_a f_a}$, which occurs for some axion-like particles, (it is equivalent to $n = 0$).

3.2 Axion Miniclusters

After t_0 , the density perturbations grow under gravity as usual, eventually collapsing into the gravitationally bound objects known as miniclusters. The characteristic minicluster mass, M_0 is set by the total mass of axionic DM contained within the horizon at time t_0 , given by

$$M_0 = \bar{\rho}_a \frac{4}{3} \pi \left(\frac{\pi}{k_0} \right)^3 \quad (3.4)$$

where k_0 is the comoving wave number associated with the horizon size at the time t_0 , $k_0 = \mathcal{H}(t_0) = a(t_0)H(t_0)$ is the conformal Hubble rate and $\bar{\rho}_a$ is the current axion density

The minicluster characteristic density, ρ_{MC} , is another important quantity, since it sets the typical radius of a minicluster, thus its concentration. The characteristic density is given in terms of the initial overdensity parameter, δ , by:

$$\rho_{MC} = 40\delta^3 (1 + \delta) \bar{\rho}_a(z_{eq}) \quad (3.5)$$

Miniclusters, once initially formed, go on to merge into larger bound structures, which can be called “minicluster halos,” or MCHs.

MCHs are small-scale structures; they are substructures within the larger-scale DM halos formed by the scale invariant adiabatic initial conditions on large scales.

3.3 Constraining Minicluster Mass Function

Fixing the DM density $\Omega_{DM} h^2 = 0.12$ determines an n -dependent relationship between m_a and f_a such that $M_0 = M_0(m_a, n)$.

For inflation theories, the empirical constraint on the cosmic microwave background tensor to scalar ratio of $r \approx 0.07$ means that this scenario for symmetry

breakdown is only viable for $f_a \lesssim 8.2 \cdot 10^{12}$ GeV.

This upper limit on f_a allows us to get a non-trivial lower limit on m_a for different n .

Before beginning with constraining the minicluster mass, we take a small detour to revise an important concept, scaling of energy density with Universal expansion.

3.3.1 Universal Expansion

The Friedmann equations are fundamental equations in ΛCDM cosmology, describing the expansion of the universe by defining a scale factor, $a(t)$.

$$H^2 = \left(\frac{\dot{a}}{a} \right)^2 = \frac{8\pi G}{3}\rho - \frac{k}{a^2} + \frac{\Lambda}{3} \quad (3.6)$$

$$\frac{\ddot{a}}{a} = -\frac{4\pi G}{3} \left(\rho + \frac{3p}{c^2} \right) + \frac{\Lambda}{3} \quad (3.7)$$

These can be solved using equations of state relating the p and ρ , for the more dominant component at a time: radiation, matter or the Cosmological constant.

Remember that as the Universe expands, it cools adiabatically and thus the Temperature of the Universe (Relativistic components) drops. So the scale factor can also be related to temperature by the condition of constant Entropy, given by:

$$a(T) \propto (g_{*,S}(T))^{-1/3} T^{-1} \quad (3.8)$$

and also in a Radiation dominated era:

$$H(T)^2 = \frac{\pi^2}{90M_{PL}^2} g_{*,R}(T) T^4 \quad (3.9)$$

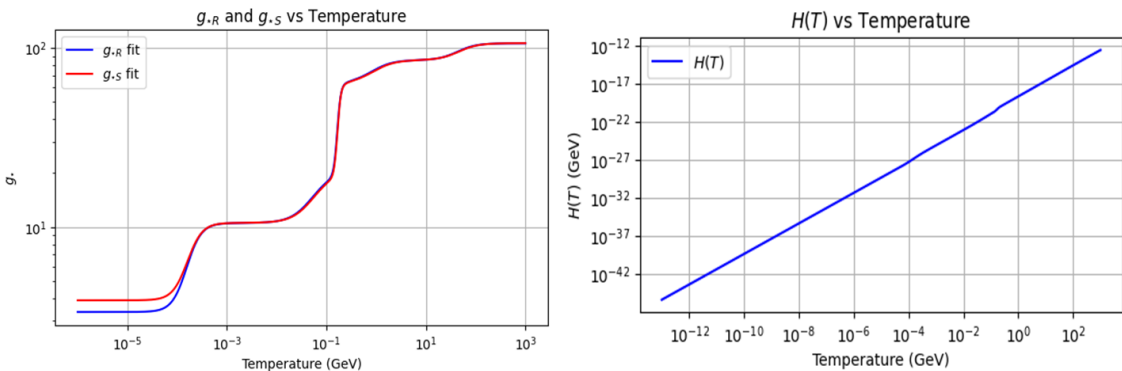


Figure 3.2: $g_{*,S}(T)$, $g_{*,R}(T)$ obtained from approx. fits provided in Wantz and Shellard (2010)

3.3.2 Calculating T_{osc}

From Eq.(3.2):

$$3H(T_{osc}) = m_a(T_{osc})$$

Now using Eq.(3.3) and Eq. (3.9), we can obtain T_{osc} for different values of m_a

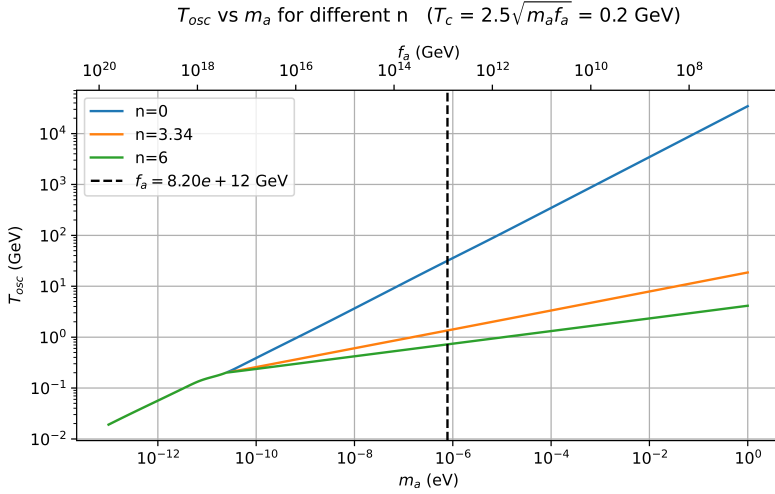


Figure 3.3: T_{osc} vs m_a & f_a for n : (0, 3.34, 6) with an assumed constant phase transition temperature: $T_c = 2.5\sqrt{m_a f_a} = 0.2$ GeV. We also impose the upper bound on f_a , left to which are scenarios not viable to form Miniclusters

3.3.3 Relating F_a and m_a

Axion oscillations begin at temperature T_{osc} when the potential term dominates over the friction provided by the Hubble expansion.

Once axion oscillations begin, the axion number density $n_a(T) = \rho_a(T)/m_a(T)$ becomes conserved(for slow m_a variation).The axion relic density at a later time, when the temperature is T_0 is then given by

$$\rho_a^{\text{mis}} = m_a(T_0)n(T_{osc}) \left(\frac{a(T_{osc})}{a(T_0)} \right)^3 = \frac{1}{2} m_a(T_0)m_a(T_{osc})f_a^2 \theta_i^2 \left(\frac{a(T_{osc})}{a(T_0)} \right)^3$$

With the assumption of constant g during the epoch over which anharmonic corrections affect T_{osc} , this solution can be found analytically, leading to an anharmonic correction to the relic density:

$$\rho_a^{\text{mis}} \rightarrow f_{an}(\theta_i)\rho_a^{\text{mis}}$$

In the minicluster scenario the vacuum misalignment relic density must be averaged over θ_i , reflecting the fact that the current observable Universe is many times larger than the horizon size when axion oscillations begin. One must replace $\theta_i^2 f_{an}(\theta_i)$ by

$$\langle \theta_i^2 f_{an}(\theta_i) \rangle = \frac{1}{2\pi} \int_{-\pi}^{\pi} \theta^2 f_{an}(\theta) d\theta \equiv c_{an} \frac{\pi^2}{3}$$

for the cosine potential and $n = (0, 3.34, 6)$, we find $c_n = (2.7, 2.1, 2.0)$, and since

$$\Omega_a = \frac{\rho_a}{3H^2 M_{pl}^2} \quad \text{and} \quad \Omega_a h^2 = (1 + \alpha_{\text{dec}}) \Omega_a^{\text{mis}} h^2$$

where $\alpha_{\text{dec}} = 2.48$, computed from the numerical solution of the decay of the axion string-wall network

Now, combining the mentioned equations, we finally reach:

$$\Omega_{\text{total}}^a = \frac{1}{6H_0^2 M_{\text{pl}}^2} (1 + \alpha_{\text{dec}}) \cdot \frac{c_{\text{an}} \pi^2}{3} \cdot m_a(T_{\text{CMB}}) \cdot m_a(T_{\text{osc}}) \times \left(\frac{a(T_{\text{osc}})}{a(T_{\text{CMB}})} \right)^3 \cdot f_a^2 \quad (3.10)$$

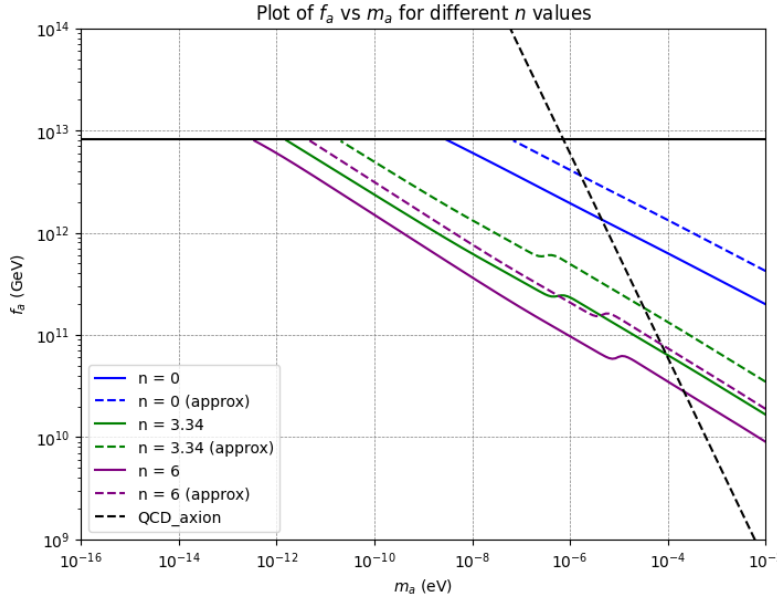


Figure 3.4: The axion relic density contours $\Omega_a h^2 = 0.12$ are shown for various n . Solid (dashed) lines have $\alpha_{\text{dec}} = 2.48(1)$ and $c_{\text{an}} = c_n(1)$. The black line indicates the upper limit $f_a = 8.2 \times 10^{12}$ GeV.

This plot is a reproduction of Figure 19 in Fairbairn. et. al. PRD 97, 083502 (2018)

3.3.4 Calculating Minicluster Mass

Now Knowing the f_a to m_a relation, we can finally find the Mass of Axion miniclusters on formation, M_0 , using Eq.(3.4).

First we calculate T_0 , which is the temperature that defines the time when the axion field goes from having an equation of state $w = 1$ to $w = 0$, we take $T_0 \approx T_{\text{osc}}$, using which we calculate $k_0 = \mathcal{H}(t_0) = a(t_0)H(t_0)$

Thus we can finally plot The characteristic minicluster mass M_0 as a function of the axion mass m_a for different temperature evolutions of the axion mass, parameterized by index n .

We use $\bar{\rho}_a = \Omega_a \times \rho_{\text{crit}}$.

and the critical density of the universe today, is taken to be $\rho_{\text{crit}} = 9.47 \times 10^{-27}$.

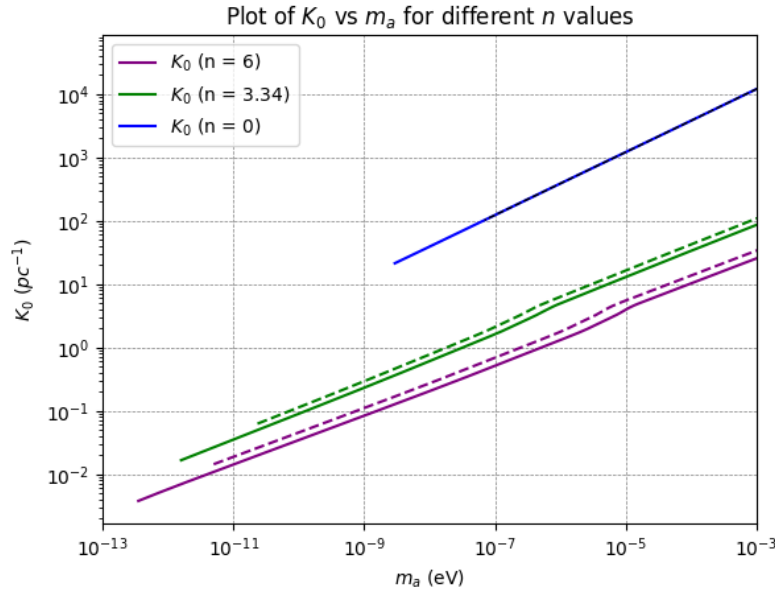


Figure 3.5: k_0 , this depends on the temperature evolution of the mass as parametrized by n and on details of the relic density computation
 This plot is a reproduction of Figure.3 in Fairbairn. et. al. PRD 97, 083502 (2018)

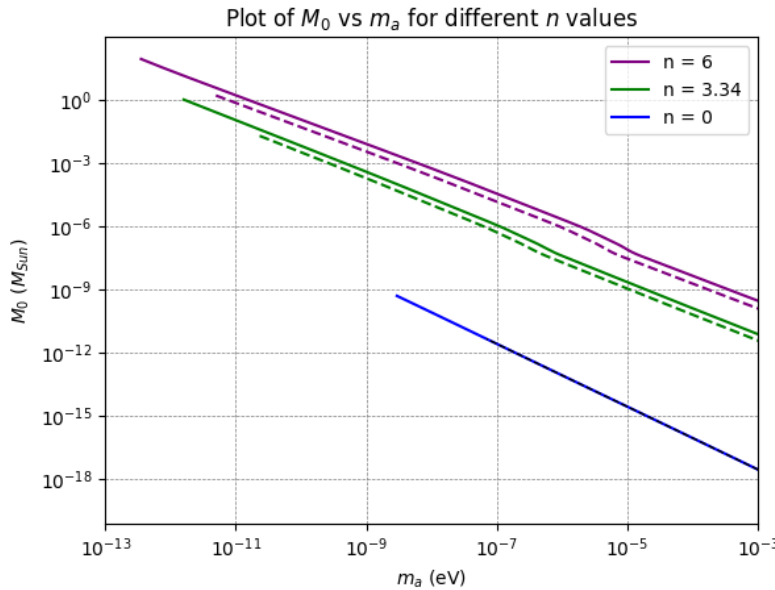


Figure 3.6: The characteristic minicluster mass: Solid lines show the most realistic assumptions about the relic density, while dashed lines are relaxed slightly. When m_a is temperature independent($n = 0$), the two cases are equivalent for M_0 . Lines terminate at a lower bound on , set by figure 3.4
 This plot is a reproduction of Figure.1 in Fairbairn. et. al. PRL 119, 021101 (2017)

3.4 Mincluster Density Functions

The scale of miniclusters is determined by $k_0 \ll k_J$, implying that their density profiles are expected to follow the cold dark matter (CDM) paradigm. The density profiles that emerge from hierarchical structure formation in CDM are well described by the well-known **Navarro-Frenk-White (NFW) profile**:

$$\rho_{\text{NFW}}(r) = \frac{\rho_s}{\frac{r}{r_s} \left(1 + \frac{r}{r_s}\right)^2}, \quad (3.11)$$

where $r_s = \rho_{\text{crit}} \delta_{\text{char}}$ is the scale radius.

However, miniclusters closer to their characteristic mass are unlikely to form through hierarchical structure formation but rather from a more direct collapse mechanism as discussed. It has been proposed that a more appropriate profile for the initial seed miniclusters could be described by **self-similar infall (SSI) profile**:

$$\rho_{\text{ssi}}(r) = \rho_s \left(\frac{r_s}{r}\right)^{9/4} \quad (3.12)$$

Such a power-law profile has also been observed in minicluster N-body simulations. For both the NFW and self-similar profiles, it is necessary to associate the density ρ_{MC} with the characteristic density and also find an integration upper limit, r_{max} :

1. In the case of the NFW profile, we simply equate $\rho_{\text{MC}} = \rho_{\text{crit}} \delta_{\text{char}} = \rho_s$ as mentioned above and rescale r_s to obtain the correct mass of the halo at r_{max} . We make the approximation that the NFW profile is cut off at a radius $r_{\text{max}} = 100r_s$.
2. The situation is slightly more complex for the self-similar profile due to the degeneracy between r_s and ρ_s caused by scale invariance. The total mass of a halo truncated at a radius r_{max} is given by

$$M = \frac{16\pi}{3} \rho_s \cdot r_s^{9/4} \cdot r_{\text{max}}^{3/4} \equiv \frac{4\pi}{3} \rho_{\text{av}} \cdot r_{\text{max}}^3 \quad (3.13)$$

with an average density of

$$\rho_{\text{av}} = 4\rho_s \left(\frac{r_s}{r_{\text{max}}}\right)^{9/4}$$

and then identify $\rho_{\text{av}} = \rho_{\text{MC}}$. We can express r_{max} as

$$r_{\text{max}} = \left(\frac{3M}{4\pi\rho_{\text{MC}}}\right)^{1/3} \quad \text{and} \quad \rho_s \cdot r_s^{9/4} = \frac{1}{4} \rho_{\text{MC}} \cdot r_{\text{max}}^{9/4} \quad (3.14)$$

3.4.1 Surface Density Profile $\Sigma(R)$

The surface density $\Sigma(R)$ is the projection of the 3D density profile $\rho(r)$ onto a 2D plane. It is obtained by integrating the 3D density $\rho(r)$ along the line of sight (perpendicular to the plane).

The surface density $\Sigma(R)$ can be calculated by:

$$\Sigma(R) = 2 \int_0^{\sqrt{R_{\max}^2 - R^2}} \rho \left(\sqrt{R^2 + z^2} \right) dz \quad (3.15)$$

where R is the 2D radial coordinate, and z is the line-of-sight coordinate. For each value of R , We integrate the 3D density profile along the line of sight from $z = 0$ to $z = \sqrt{r_{\max}^2 - R^2}$.

3.4.2 Cumulative Mass Profile $M(< R)$

The cumulative mass $M(< R)$ is the total mass enclosed within a radius R in the projected 2D plane.

The cumulative mass $M(< R)$ is given by:

$$M(< R) = 2\pi \int_0^R \Sigma(R') R' dR' \quad (3.16)$$

where $2\pi R' \Sigma(R')$ is the Mass inside the Ring with radius $R' + dR'$

This integral sums up the mass within concentric rings of radius R' to give the total mass inside R .

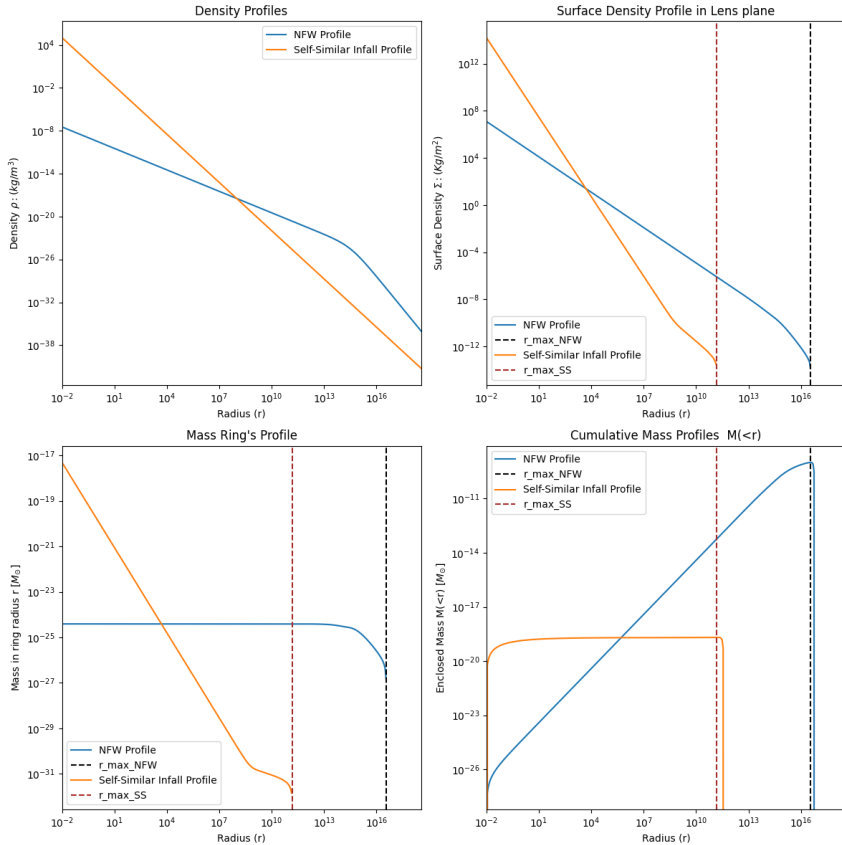


Figure 3.7: The Minicluster Density, Surface Density and Cumulative Mass functions for NFW and SSI Density Profiles as a function of radius r from the center of the Minicluster. The minicluster has a total mass of $10^{-9} M_\odot$. The SSI Cumulative mass Function has some error and does not end at the desired total mass.

3.5 Theroetical uncertainties in the MCH mass function and analytic results

We will address three theoretical uncertainties in our modelling of the MCH mass function:

- (i) The initial power spectrum to model the effects of the Kibble mechanism, $P(k_0, \tau_0)$
- (ii) The filtering function to define the mass variance, $W(kR)$
- (iii) The cutoff of the mass function

We define the mass: $M = (2\pi)^{3/2} \bar{\rho}_{a,0} R^3$ and compute the variance, $\sigma^2(M)$, at the initial time, τ_0 . We consider two simplified models for the initial power spectrum:

$$P_G(k) = P_{0,G} \exp \left[-\frac{1}{2} \left(\frac{k}{k_0} \right)^2 \right], \quad P_{0,G} = \frac{8\sqrt{2}}{5} \pi^{3/2} k_0^{-3}$$

$$P_H(k) = P_{0,H} \Theta(k_0 - k), \quad P_{0,H} = \frac{24}{5} \pi^2 k_0^{-3}$$

with G for Gaussian and H for Heaviside. In addition to the power spectrum, we also consider two choices of window function:

$$W_G^2(kR) = e^{-k^2 R^2}$$

$$W_H^2(kR) = \Theta(1 - kR)$$

For all combinations of initial power and window function the variance can be expressed analytically, in terms of error functions where necessary. We write the variance as σ_{XY}^2 , where X and Y take on either of the values G and H, with X labeling the window function and Y labeling the initial power spectrum using:

$$\sigma^2(R) = \int \frac{dk}{k} \frac{k^3 P(k)}{2\pi^2} |W(kR)|^2$$

We consider the formation of gravitationally bound structures from linear density perturbations using the analytic Press-Schechter formalism. The quantity δ_c is the critical overdensity threshold for gravitational collapse and plays a key role in the Press Schechter formalism. In spherical collapse of cold dark matter it is given by $\delta_c \approx 1.686$, and it is scale independent.

For every point in space, the probability to have $\delta > \delta_c$ using the filtered version of δ by W_M is

$$p(\delta > \delta_c | W_M) = \frac{1}{2} \left(1 - \text{erf} \left(\frac{\delta_c}{\sqrt{2}\sigma(M)} \right) \right)$$

If $n(M)$ is the number density of structures of mass M , then the halo mass function (HMF), defined by

$$\frac{dn}{d \ln M} = \frac{1}{2} \frac{\bar{\rho}_a}{M} \left| \frac{d \ln \sigma^2}{d \ln M} \right| \sqrt{\frac{2}{\pi}} \frac{\delta_c}{\sigma} \exp \left[-\frac{1}{2} \left(\frac{\delta_c}{\sigma} \right)^2 \right]$$

We also fit half-mode cutoff:

$$\frac{dn}{d \ln M} \rightarrow \left[1 + \left(\frac{2.4M}{M_{1/2}} \right)^{-1.1} \right]^{-2.2} \frac{dn}{d \ln M}$$

We obtain the following plots for the RMS mass fluctuations, and Press-Schechter mass function:

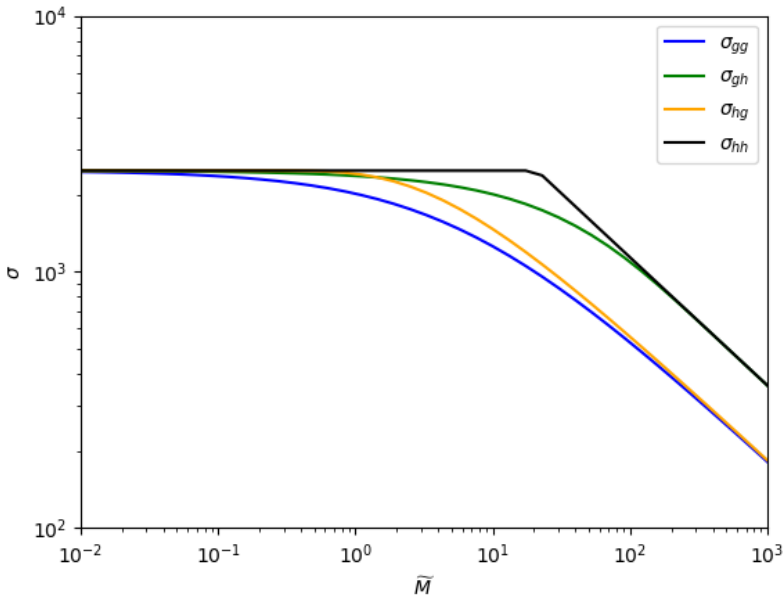


Figure 3.8: Theoretical modeling of the rms. The mass fluctuation, σ , is shown as a function of mass for four different combinations of initial power spectrum and window function. The Gaussian initial power cuts off power earlier than the step function. The Heaviside window function leads to a more pronounced flattening of σ at low masses. The reduced mass $\tilde{M} = M k_0^3 / \bar{\rho}_a$.

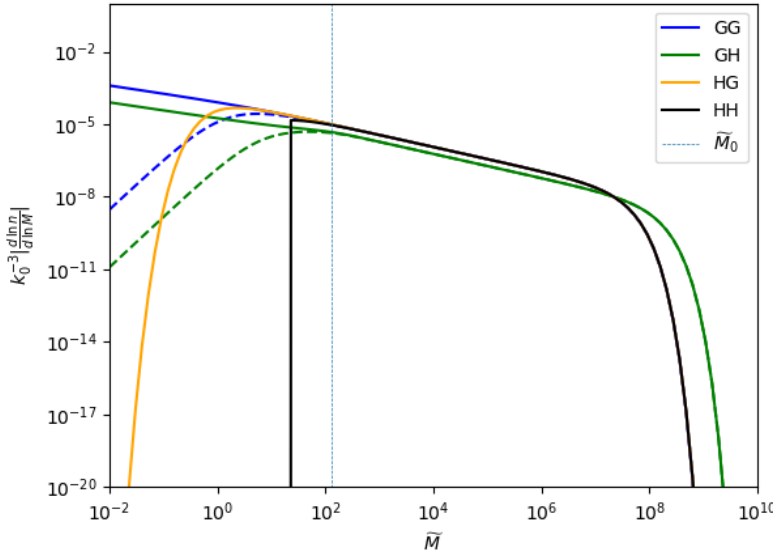


Figure 3.9: Theoretical modelling of the mass function. The minicuster mass function is shown as a function of mass for four different combinations of initial power spectrum and window function. In this case of the Gaussian window function, we also show the uncut (solid) and half-mode (dashed) models for the low-mass cutoff. The reduced mass $\tilde{M} = M k_0^3 / \bar{\rho}_a$.

Bibliography

Articles

Malcolm Fairbairn, David J. E. Marsh, Jérémie Quevillon, and Simon Rozier
Phys. Rev. D 97, 083502 (2018)

Malcolm Fairbairn, David J.E. Marsh, and Jérémie Quevillon
Phys. Rev. Lett. 119, 02110

Ramesh Narayan (Gravitational Lensing Review)
arXiv:astro-ph/9606001v2 2 Oct 1997

Chadha-Day et al. ,
Sci. Adv. 8, eabj3618(2022)

Ciaran A. J. O'Hare
Cosmology of Axion Dark Matter

Elisa G. M. Ferreira (Ultra Light Dark Matter)
arXiv:2005.03254v2 (astro-ph.CO) 3 Feb 2021

Ann E. Nelson and Huangyu Xiao (Axion cosmology with early matter domination)
Phys. Rev. D 98, 063516 - 13 September 2018

Olivier Wantz and E. P. S. Shellard (Axion cosmology revisited)
Phys. Rev. D 82, 123508 - 2 December 2010

Roszkowski, L., Sessolo, E. M., & Trojanowski, S. (WIMP dark matter candidates and searches - current status and future prospects)
arXiv:1707.06277v2 19 July 2017.